

Parametric Geometry, Structured Grid Generation, and Initial Design Study for REST-Class Hypersonic Inlets*

Paul G. Ferlemann
ATK, Space Systems Group
Hampton, Virginia

Rowan J. Gollan
NIA, Visiting Researcher
Hampton, Virginia

ABSTRACT

Computational design and analysis of three-dimensional hypersonic inlets with shape transition has been a significant challenge due to the complex geometry and grid required for three-dimensional viscous flow calculations. Currently, the design process utilizes an inviscid design tool to produce initial inlet shapes by streamline tracing through an axisymmetric compression field. However, the shape is defined by a large number of points rather than a continuous surface and lacks important features such as blunt leading edges. Therefore, a design system has been developed to parametrically construct true CAD geometry and link the topology of a structured grid to the geometry. The Adaptive Modeling Language (AML) constitutes the underlying framework that is used to build the geometry and grid topology. Parameterization of the CAD geometry allows the inlet shapes produced by the inviscid design tool to be generated, but also allows a great deal of flexibility to modify the shape to account for three-dimensional viscous effects. By linking the grid topology to the parametric geometry, the GridPro grid generation software can be used efficiently to produce a smooth hexahedral multiblock grid. To demonstrate the new capability, a matrix of inlets were designed by varying four geometry parameters in the inviscid design tool. The goals of the initial design study were to explore inviscid design tool geometry variations with a three-dimensional analysis approach, demonstrate a solution rate which would enable the use of high-fidelity viscous three-dimensional CFD in future design efforts, process the results for important performance parameters, and perform a sample optimization.

INTRODUCTION

A significant amount of interest exists in the design of three-dimensional vehicle-integrated hypersonic inlets which produce an efficient compression of the core flow while also maintaining well-behaved boundary layer characteristics. Well-behaved refers to lack of flow separation, significant non-uniformity, boundary layer roll-up, or other viscous effects which might limit back pressure capability or robust operation over the desired speed range. Inlet design techniques based on streamline tracing emphasize efficiency of the inviscid core compression and usually apply an approximate viscous correction. However, the complexity of the three-dimensional viscous interaction invalidates the small crossflow assumption and renders such a correction inadequate. The resulting inlets typically suffer from significant viscous effects when a fully-coupled solution technique is applied and the expected performance is not realized. In addition, empirically developed isolator correlations rely on local boundary layer properties and predict relatively low back pressure capability. Therefore, the inability to fully account for boundary layer development with an uncoupled design approach and the desire to include robust operation as part of an optimization provide the motivation to use high-fidelity viscous three-dimensional computational fluid dynamics (CFD) as a design tool for various types of inlets.

The flow analysis paradigm for this work originates from the requirement to design using a high-fidelity tool (physical models and grid resolution equivalent to final design evaluation fidelity). In addition, any realistic design activity potentially involves a large number of variables, initially unknown or poorly defined constraints, and a complex and possibly changing optimization function. Consequently, numerous solutions are required, must be generated at a reasonable rate, and require the minimization of human involvement in the generation of results. Therefore, a process to rapidly create parametric computer-aided design (CAD) geometry and structured grids for CFD analysis has been identified. The first three-

* Approved for public release; distribution is unlimited.

* This work was supported by the NASA Fundamental Aeronautics Program, Hypersonics Project through contract NNL07AA00B with the NASA Langley Research Center.

dimensional hypersonic inlet type selected to demonstrate the new capability was the Rectangular-to-Elliptical Shape Transition (REST) inlet.¹ An initial design study was performed using inviscid design tool geometry variables. The objectives were to drive the development of the parametric geometry and structured grid generation and to generate data to assess performance metrics for optimization. In particular, quantify viscous effects in various ways and demonstrate the capability to determine the cause and effect relationship with design variables. A Modern Design of Experiments methodology was used to minimize the number of solutions required and to help in the interpretation of the results. A sample optimization was performed to illustrate the ability to handle multiple performance parameters. As is typically the case, all of the performance parameters could not be optimized simultaneously and displayed a range of sensitivity to the independent variables.

THREE-DIMENSIONAL INLET DESIGN METHOD

The design intent of a REST-class hypersonic inlet is to produce the final amount of compression efficiently over a Mach number range with a fixed, but shape transitioning, geometry. Two views of three REST inlets are shown in Figure 1. The concept takes advantage of a two-dimensional class of forebody (not shown) to provide external compression and to make the flow angle entering the inlet insensitive to vehicle angle-of-attack. The shape transitions from a rectangular-like capture shape (planar forebody and vertical splitter leading edges) to an ellipse at the inlet exit. The capability to create super-elliptical throat shapes has been added to the design method. If the throat aspect ratio equals one, a rounded square or circular throat shape can be produced. Currently, for design purposes the inlet geometry is symmetrical with no lateral component to the inflow. Therefore, half of one inlet is analyzed in CFD simulations.

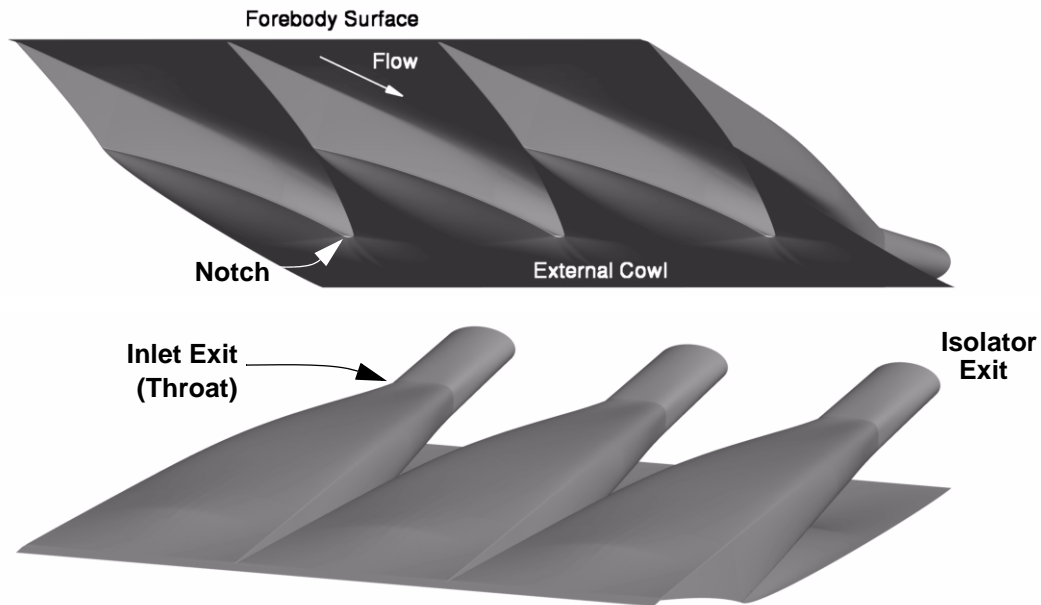


Figure 1. Modular REST inlets.

The design method for a REST inlet presented by Smart¹ can be separated into two parts: 1) the generation of an inviscid inlet based on streamline tracing, and 2) the application of an approximate viscous correction. The first part of the design can be further divided into a number of steps:

1. Produce an axisymmetric compression field for the required Mach number and pressure ratio.
2. Generate a stream-traced inlet using a rectangular-like capture shape (shape A).
3. Generate a second stream-traced inlet shape using a capture shape similar to the first shape but with rounded corners (shape B).
4. Generate a third inlet shape (shape C) with an elliptical throat area equal to the throat area of shape A.

5. Smoothly blend all three inlet shapes to form a three-dimensional inlet that has shape A as the capture shape, the cross-sectional shape of shape B at cowl closure (notch), and the elliptical throat of shape C.

Therefore, the inlet is not truly streamline-traced because of the blending process, but it is based on streamline-tracing techniques.

GENERATION OF AN AXISYMMETRIC COMPRESSION FIELD

The generation of an axisymmetric compression field is central to the inlet design process. There are several desirable features for the compression field: maximum total pressure recovery, constrained maximum shock strength that will not induce boundary layer separation, minimum length and minimal exit flow nonuniformity. The actual compression field is a compromise based on these desirable features. It is also useful to include a constant radius centerbody in the compression field to avoid high losses associated with shock focusing at the axis. Given the set of trade-offs mentioned above, there is no unique choice for the axisymmetric compression field for a given inlet design. A suggested method to create a compression field is as follows. First, calculate an expanding flowfield (a nozzle contour) with a similar throat Mach number and pressure ratio to the desired inlet properties. Second, reverse the flowfield and shorten the contour by introducing a non-zero lip angle, that is, truncate the contour.

STREAMLINE-TRACING WITH BLENDING TO BUILD INLET

Once an axisymmetric compression field is obtained, the streamline-tracing process produces three inlets (or stream tubes) as described in steps 2, 3, and 4 above. The inviscid inlet surface is built from two blending processes. The surface from the inlet entrance to the notch results from blending shapes A and B. The surface from the notch to the throat results from blending shapes B and C. The blending technique is based on the procedure proposed by Barger.² If each cross-section is parameterized as some function of y , then the blended values for shapes A and B are computed as:

$$f(y) = [f_A(y)]^{1-E(x)} [f_B(y)]^{E(x)} \quad \text{where} \quad E(x) = \left(\frac{x - x_{ca}}{x_n - x_{ca}} \right)^\alpha \quad \text{and} \quad \alpha > 0 \quad (1)$$

In the above, f_A and f_B are values from shapes A and B respectively, x_{ca} is the location of capture, and x_n is the location of the notch. A similar expression may be written for blending shapes B and C, for the surface from the notch to the throat. Smart found that values of α between 1 and 5 produced sensible shape transitions where a larger value favors or maintains the front shape longer and a smaller value favors the back shape.¹ For this study, $\alpha_{A-B}=1.6$ for all cases based on previous experience. In contrast, the notch-to-throat shape transition for a low throat aspect ratio (rounded square or circular inlet exit) had to strongly weight shape C to achieve a sensible design while more uniform weighting was preferred for higher throat aspect ratios. Therefore, α_{B-C} was set equal to the throat aspect ratio.

APPROXIMATE VISCOUS CORRECTION TO INLET SURFACE

The initial blended inlet surface is based on an inviscid flowfield. In practice, boundary layer growth will reduce the core flow area and lead to a higher effective contraction ratio than intended. Therefore, the surface is enlarged by considering the development of the boundary layer along initial surface streamlines. The computed boundary layer displacement thickness is smoothed and added to the inviscid inlet to produce the final inlet surface which is intended to produce a core flow shape similar to the initial blended surface shape. However, performing boundary layer calculations along inviscid surface streamlines does not account for the fully coupled character of the flowfield. In particular, the boundary layer provides a mechanism for pressure gradients to be communicated circumferentially around the inlet. As a result, the small crossflow assumption is not reasonable. The general effect is that current designs can have good total pressure recovery based on one-dimensionalized flow properties, but this does not necessarily lead to good back pressure capability. Empirically developed isolator correlations limit the predicted maximum back pressure based on local boundary layer properties. Therefore, the inability to fully account for boundary layer development with an uncoupled design approach and the desire to optimize for robust operation provide the motivation for using high-fidelity viscous three-dimensional CFD as a design tool in the future.

PARAMETRIC COMPUTER-AIDED DESIGN (CAD) GEOMETRY GENERATION

Prior to grid generation, the geometry must be represented as a continuous surface. In order to create a complex surface with CAD, the surface must be subdivided into separate surface patches. This is required because the primary way to achieve the desired surface shape is to control the shape of the edges. The inviscid design tool creates a cloud of points to represent the geometry. Therefore, five basic steps are required to produce parametric CAD geometry. First, identify the edges (or topology of the geometry) which are sufficient to capture the geometric features of a representative case. Second, extract a sufficient amount of information from the cloud of points to define the shape of some edges. Third, provide information to generate edges not defined by the cloud of points (for leading edge bluntness, notch radius, isolator, and external cowl). Fourth, build edges required to define surface patches using information from previously built edges so that no additional information is required. Fifth, allow flexibility in the number and types of curves used to define edges so that shapes significantly different from the initial representative case can be created. To eliminate human involvement, a system must be created so that the geometry can be automatically regenerated when a design parameter is changed. It is important to recognize that optimization of the surface will be limited to geometry variations that are possible with the selected surface topology. Therefore, there is a trade-off between attempting to keep geometry parameterization fairly simple and the complexity of the possible optimum geometry.

For a REST inlet configuration, construction of the parametric CAD geometry with the Adaptive Model Language³ (AML) is shown in Figure 2. One half of one inlet is shown. The cloud of points for a representative geometry is included as the top image (a). The first required edges form the perimeter of the inlet surface (b). The construction of this closed loop was divided into separate segments for: body centerline, throat curve, cowl internal centerline, cowl external centerline, external cowl trailing edge, external cowl edge along sidewall centerline, sidewall centerline and inlet leading edge. The order of construction was important since data dependencies have been used whenever possible. For example, the start or end of an edge is not specified if the edges to which it is connected have already been built. The external cowl trailing edge and inlet leading edge are assumed to be linear. The throat curve is a superellipse. The remaining edges can be any combination of linear or cubic Bezier curve segments. A user-friendly method of providing information to the system was used whenever possible. For example, the location of the control points for the Bezier curve segments are entered as a single weight factor which is normalized based on the chord length. Therefore, the user does not need to calculate the three-dimensional location of the control points. In addition, the input for the throat curve is: throat area and aspect ratio, shape superellipse power, and construction plane normal vector. Since the body centerline curve was constructed first, the system performs the necessary calculations to construct the throat curve. Because the cowl internal curve is generated next, the end location of the internal cowl curve is not specified and can only be moved by changing the body centerline end point or the throat curve properties. Construction of the cowl external centerline curve includes an up-turned section to allow the addition of a radius at the notch (normal to symmetry plane). In contrast, the points defining the cowl leading edge in the cloud of points approach the symmetry plane at a highly oblique angle. The next set of required edges were some cross-sectional edges called ribs (c). The first, mostly hidden in the current view, defines the start of the blunt sidewall leading edge (barely visible upper right corner). Two ribs are built near the beginning of the cowl leading edge in two basic sections. A cowl surface section is added to create the two three-piece ribs at the notch. The upstream rib includes a high curvature fold that will become the cowl leading edge and crosses the external cowl. The downstream rib begins at the beginning of the internal cowl centerline curve. The next image (d) shows the addition of the cowl leading edge internal tangency curve and corner flow curves. The cloud of points does not include the isolator. Therefore, the next image (e) shows the creation of isolator edges based on the isolator length, exit area ratio from the throat, aspect ratio, and superellipse power. The isolator exit edge is automatically built on a plane parallel to the inlet exit plane. Edges to form the inner tangency curve for the sidewall blunt leading edge and external tangency curve for the cowl leading edge are created with identical shape information as the sidewall centerline curve and cowl leading edge internal tangency curve, respectively. The final image (f) shows the lofted CAD surface shaded grey and compared to the original cloud of points. For this example, the maximum difference was 0.16 inches (0.3% of total length or 5 times the blunt leading edge radius) and occurred near the corner between the body and the sidewall. The difference was considered small enough

so that the selected topology for the geometry was sufficient. Therefore, the surface was not created based on all of the points (~10,000) in the cloud. Rather, the coordinates of key points, curve fitting of edges, slopes of ribs, and additional information (for bluntness, notch radius, isolator, and external cowl) were used to create the CAD geometry. This was done to drastically reduce the amount of information required so that the shape could be controlled with a reasonable number of parameters while still accurately reproducing the initial representative shape. Although more complex edge generation is possible, the input specification for the parametric CAD geometry contained 107 parameters. However, the 36 Bezier curve control points have a relatively subtle effect for desirable gently curving edges. Therefore, a complete optimization study would require ~70 independent variables.

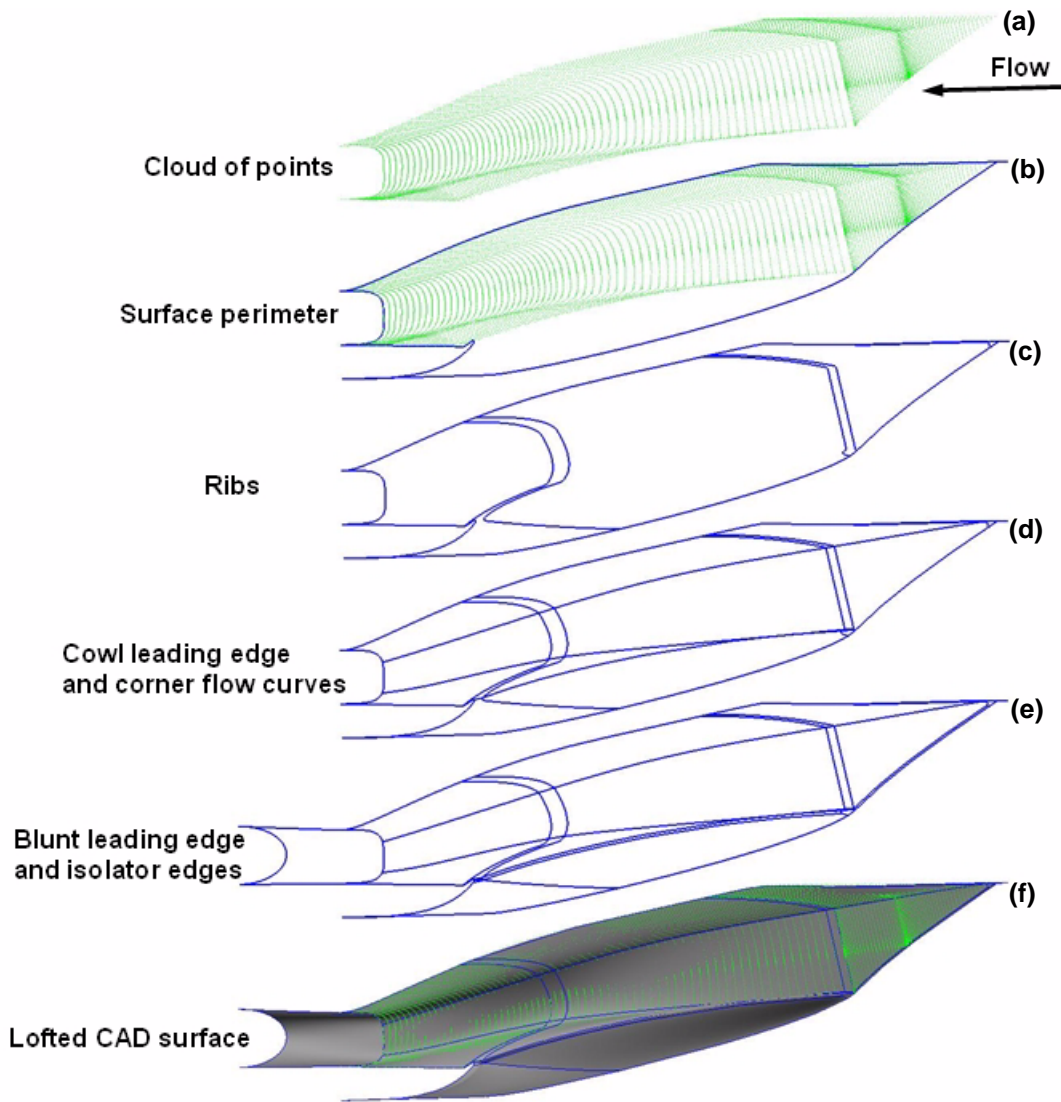


Figure 2. Development of parametric CAD geometry.

GRID GENERATION

GridPro⁴ grid generation software focuses human effort on creating the block topology, or the wire frame, created by the block edges. While each grid block must be structured (8 corners and 6 faces), they can be connected in an unstructured way. In two dimensions, this means that 3 or 5 edges could share the same corner point, rather than the usual 4 edges. Such points are referred to as singularities and are best used only when necessary to achieve the desired grid flow. Once a topology is created, the grid solver produces a grid which conforms to the geometry and maintains a relatively equal cell size and aspect ratio

outside of the boundary layer. The created topology is shown in Figure 3. The topology primarily consisted of block corners defined at the sidewall start, mid-point of the sidewall, cowl start corner, midpoint of the cowl, notch, inlet exit, and isolator exit. Grid topology singularities on the surface were limited to the start of the sidewall, start of the cowl, middle of the external cowl, and on the interior and exterior surfaces at the notch. Due to the high curvature created by the blunt leading edges and twisting required by some blocks, the behavior and results of the GridPro grid solver were significantly affected by the initial block corner locations. Therefore, although the topology remained constant conceptually, the corner locations were adjusted to the geometry for each case. While this was done manually for this study, generic structured grid topology construction software has now been developed in AML so that the grid topology can be linked to the geometry. Therefore, a change to the parametric geometry will regenerate both the surface geometry and the structured grid block topology, further streamlining grid generation in the future. Since the corners were positioned properly before executing the GridPro solver, it only had to project the surface grid to the geometry and perform a fairly small amount of smoothing. Only 500 iterations, or about 2 minutes, were required (single 2.33 GHz processor). An inviscid cell dimension of 0.2 inches or less was selected to adequately resolve hypersonic inlet flow physics. GridPro utilities were used to add boundary layer points with a near wall spacing of 0.0005 inches to achieve a y^+ of approximately one for most of the model and to merge the 290 elemental blocks into 17 superblocks. Gridgen⁵ was used to perform final grid preparation. This involved: changing near-wall spacing at the forebody blunt leading edge stagnation point, block reorientation, splitting blocks into separate laminar and turbulent regions, and splitting blocks for parallel processing. Each case had 2.7 million cells.

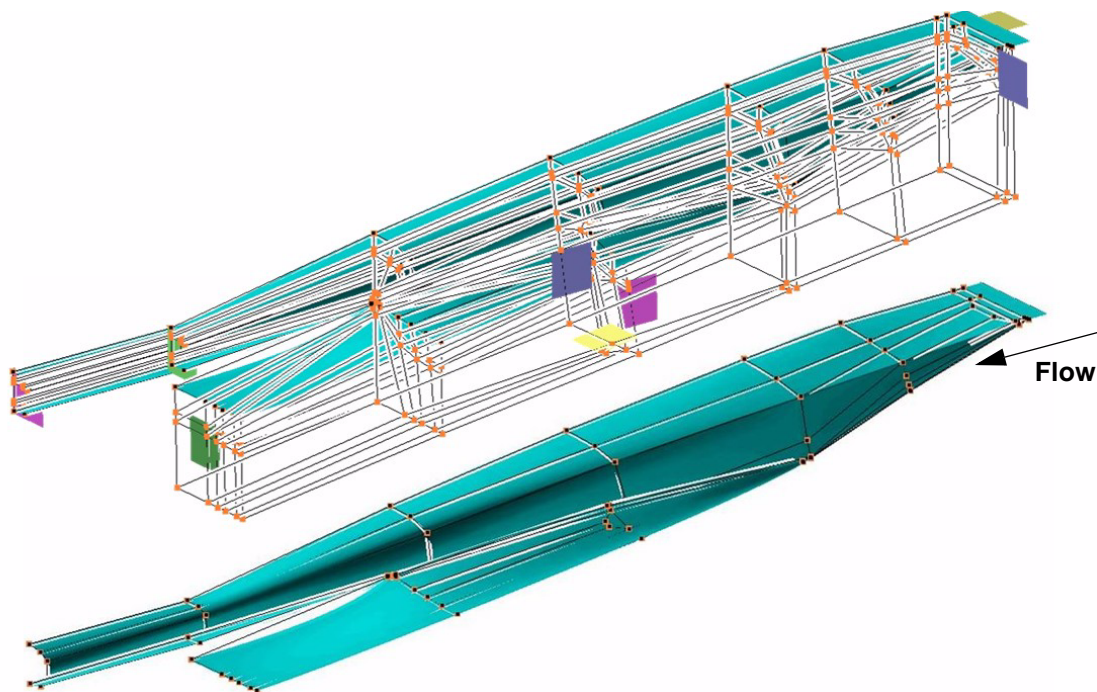


Figure 3. Structured grid block topology (top – complete volume, bottom – surface only).

INITIAL THREE-DIMENSIONAL HYPERSONIC INLET DESIGN STUDY

INLET DESIGN SPECIFICATIONS

The target for the inlet design matrix was an overall compression ratio of 37.55 with inflow conditions of $M_\infty = 7$ and $q_\infty = 1730$ psf to match the HIFiRE 2⁶⁻⁷ design and trajectory so that comparisons could be made with a different class of inlet. However, no comparisons will be presented in this paper. The shape-transition inlet was modeled at zero degrees angle of attack. Therefore, in this study the inlet inflow conditions were equal to the freestream conditions. The aspect ratio of the isolator exit was matched to the inlet exit aspect ratio. The isolator exit was constrained to be a true ellipse. For cases with a superellipse shape at the inlet exit, this produced a constant area shape transition through the isolator.

INDEPENDENT VARIABLES

Four geometric variables which could be controlled with the inviscid design tool were selected as independent variables. These were the lip angle, the capture aspect ratio, the throat aspect ratio, and the throat shape. The selected range for each variable is listed in Table 1.

Table 1. Independent variables.

Variable	Low	Mid	High
Lip Angle	4.5°	5.0°	5.5°
Capture Aspect Ratio	1.27	1.41	1.55
Throat Aspect Ratio	1.0	1.75	2.5
Throat Superellipse Power	2	4	6

The lip angle refers to the angle at which the inlet surface first begins to deviate from the forebody as shown in Figure 4. As discussed previously, this parameter controls the level of truncation imposed on the compressive flowfield used for streamline tracing. The range was selected based on previous design experience with this class of inlet. In this study, with the forebody at zero degrees angle of attack, the lip angle controlled the initial turning seen by the flow (ignoring forebody blunt leading edge effects and initial boundary layer development). Therefore, the lip angle had a direct influence on the amount of shock compression used to compress the flow. It also affected the inlet length.

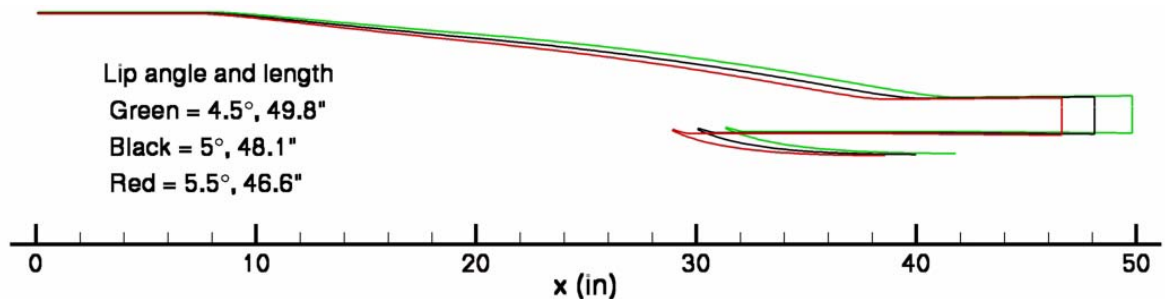


Figure 4. Centerline geometry variation with lip angle.

The capture aspect ratio is the width-to-height ratio of the rectangular-like shape that forms the capture area of the inlet. Three inlets from the design study are shown from the front looking into the inlet in Figure 5. The images include the predicted surface pressure and the external cowl surface. The middle value for this study was 1.41. This value gives the maximum capture area for the rectangular-like capture shape within the confines of the axisymmetric compression field from which the inlet was streamline-traced. The high and low values for the capture aspect ratio produced a smaller capture area compared to the mid-value for the same compression field. In order to produce the same mass capture these inlets were geometrically scaled. The capture aspect ratio variable range of 1.27 – 1.55 was not a far ranging probe of the design space. This range was limited by the choice of throat aspect ratio range. A fairly large variable range was desired for the throat aspect ratio and required a relatively small variable range for the capture aspect ratio to ensure that sensible inlet designs (reasonable wall angles) were produced at all combinations of the independent variables.

The selected range for the throat aspect ratio was 1.0 – 2.5. Figure 6 shows the variation in throat aspect ratio as well as the shape change through the isolator. The more rounded rectangular black line is the inlet exit, while the true ellipse (or circle) is the isolator exit. The mid value of 1.75 was chosen as a reasonable compromise between structural concerns and fuel mixing requirements in the combustor. While a low aspect ratio (circular) is better for hoop strength and to minimize the duct perimeter for a given flow area, a higher aspect ratio duct reduces the fuel penetration distance required to reach all of the air. The minimum throat aspect ratio produced a circular or rounded square shaped throat. This was selected out of interest and as a test of the design tool's robustness. The circular throat shape results in a fairly extreme shape change from a large aspect ratio rectangular capture shape. A high value of 2.5 was required to maintain equal spacing between variable levels.

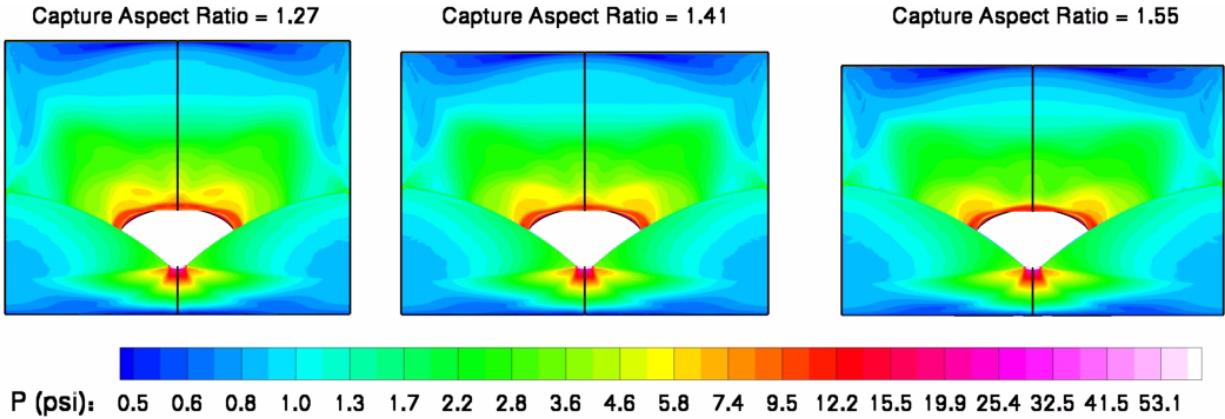


Figure 5. Front view geometry variation with capture aspect ratio.

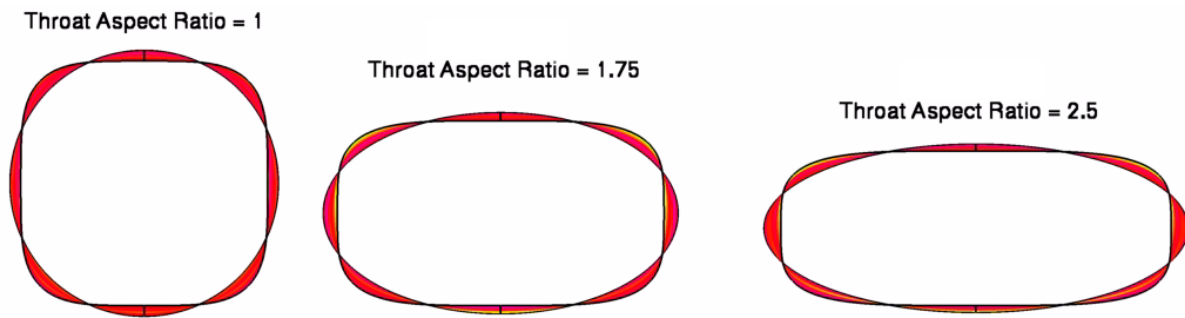
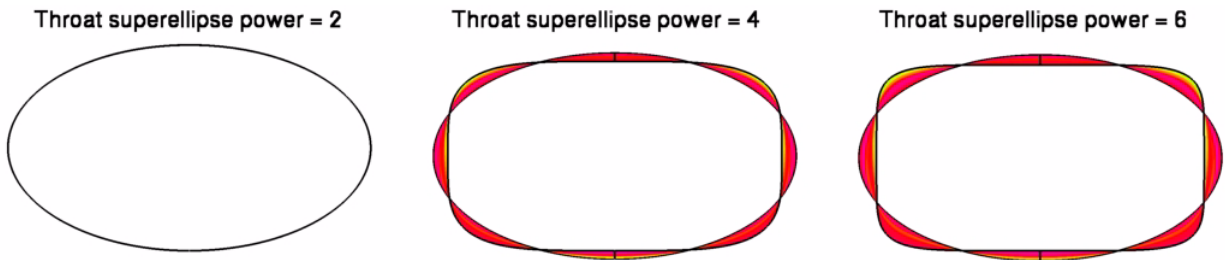


Figure 6. Inlet and isolator exit geometry variation with throat aspect ratio.

The fourth geometry variable in the design study was the inlet exit shape superellipse power. A value of 2 produced a true ellipse. At powers greater than 2, the shape became more of a rounded rectangle, as shown in Figure 7. The isolator exit was constrained to be a true ellipse. Therefore, by varying the inlet exit shape superellipse power the merits of performing all of the shape transition in the inlet could be compared to deferring some of the shape change to the isolator. The isolator surface was a CAD lofted surface constrained by the curves at the inlet and isolator exits.



Isolator exit is always a regular ellipse (power = 2).

Figure 7. Inlet exit shape sensitivity to superellipse power.

MODERN DESIGN OF EXPERIMENTS (MDOE) MATRIX

Table 2 shows the matrix of cases used to explore the design space created by the variation of four independent variables. It is a 4 variable, face centered (3 level), central composite design suitable for response surface analysis with Design Expert.⁸ A “small” matrix requiring 17 cases was selected rather than a “full” 25 case matrix. Therefore, caution must be used when assessing the derived quadratic response surfaces. The first 8 cases represent corners of the design space with every variable at a minimum or maximum value. The second 8 cases represent the faces of the design space or the sensitivity to a single variable. Case 17 is the center of the design space.

Table 2. Three-dimensional inlet design variable values.*

Case	Independent Variable (Normalized Value)				Independent Variable (Dimensional Value)				Case
	v1	v2	v3	v4	Lip Angle	Capture Aspect Ratio	Throat Aspect Ratio	Throat Ellipse Power	
1	1	1	1	-1	5.5	1.55	2.5	2	1
2	1	1	-1	-1	5.5	1.55	1	2	2
3	1	-1	1	1	5.5	1.27	2.5	6	3
4	-1	1	-1	1	4.5	1.55	1	6	4
5	1	-1	-1	1	5.5	1.27	1	6	5
6	-1	-1	1	-1	4.5	1.27	2.5	2	6
7	-1	1	1	1	4.5	1.55	2.5	6	7
8	-1	-1	-1	-1	4.5	1.27	1	2	8
9	-1	0	0	0	4.5	1.41	1.75	4	9
10	1	0	0	0	5.5	1.41	1.75	4	10
11	0	-1	0	0	5	1.27	1.75	4	11
12	0	1	0	0	5	1.55	1.75	4	12
13	0	0	-1	0	5	1.41	1	4	13
14	0	0	1	0	5	1.41	2.5	4	14
15	0	0	0	-1	5	1.41	1.75	2	15
16	0	0	0	1	5	1.41	1.75	6	16
17	0	0	0	0	5	1.41	1.75	4	17

* White= super-elliptical inlet exit and elliptical isolator exit (constant aspect ratio and area).
 Green = elliptical inlet exit and constant shape isolator.
 Red = circular inlet exit and constant shape isolator.

COMPUTATIONAL METHODOLOGY

The VULCAN⁹ CFD software version 6.0.2 was used to compute the flowfield. The air was modeled as thermally perfect. All surfaces were modeled as isothermal at 540 R. The forebody leading edge had a 0.030 inch radius. The flowfield was modeled laminar to the end of the sidewall leading edge. Downstream of this point, the k-omega turbulence model was used with wall matching functions. Most of the surface area had a y+ less than 11.5 so that near wall blending occurred with the integrate to the wall expressions. The highest y+ was ~100 and occurred at the blunt notch stagnation point. Three levels of grid sequencing were used along with Edward's Low Dissipation Flux Split Scheme and the Diagonalized Approximate Factorization solver. A second order flux reconstruction was used on the fine grid with the smooth limiter.¹⁰ With no sideslip flow angle, symmetry allowed half of the inlet to be modeled. Using 7 (3.4 GHz) processors on a Linux cluster, 20 hours of wall clock time were required for each case.

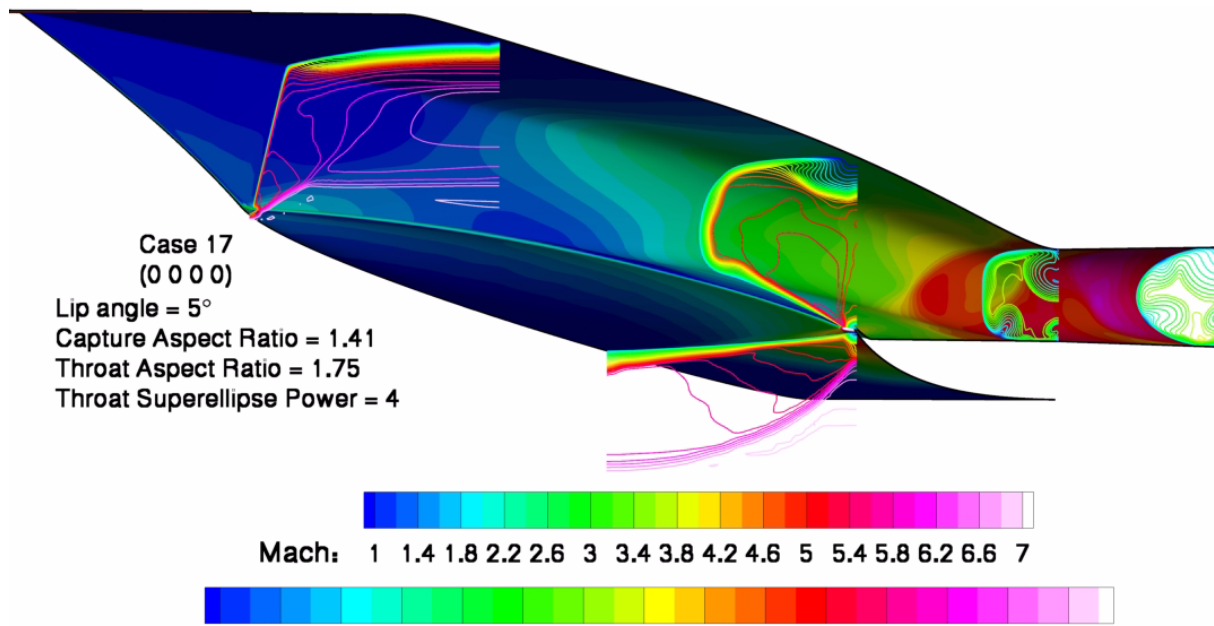
THREE-DIMENSIONAL INLET RESULTS AND DISCUSSION

Case 17 represented the center of the design space. Figure 8 includes surface pressure and Mach number contours that reveal significant boundary layer thickening along the body side centerline has occurred by the notch axial location. The shear and surface streamlines of Figure 9 show that the sidewall turns the body side surface streamlines towards the centerline and that a laminar separation occurs at the beginning of the body centerline compression. The inlet surface was not constrained to be tangent to the isolator surface and resulted in a discontinuity in the wall shear prediction at the isolator entrance. A large amount of variation in wall shear was predicted around the isolator. Figure 10 shows a cross-section of the flow at the inlet and isolator exits. The image includes Mach number contours on the left and the shaded boundary layer area, defined by 99.5% of free-stream total enthalpy, on the right. The shaded boundary layer area is divided by the total cross-sectional area and referred to as the boundary layer area ratio

(BLAR). It was tracked as a potential well-behaved viscous response which could be used for optimization. A large accumulation of boundary layer flow at the body centerline (top) was predicted at the inlet exit. There were also boundary layer “bubbles” or accumulations of low momentum flow at the cowl centerline and at the corner of the cowl and sidewall. The area consumed by boundary layer increased fairly significantly through the isolator from 60.3% to 83.1%. For the remaining cases only the Mach contours and boundary layer shape will be presented in this paper. The cases are not presented in matrix run order to make more direct comparisons between related cases. The independent design variables are repeated in each figure (Lip \leq Lip Angle, CAR = Capture Aspect Ratio, TAR = Throat Aspect Ratio, TSP = Throat Superellipse Power).

Cases 9 – 16 represent one-variable-at-a-time changes from the center of the design space. **Cases 15, 16, and 17** illustrate the effects of changing only the throat superellipse power. Case 15 has an elliptical throat shape and constant shape isolator; results are shown in Figure 11. Case 16 has the most rectangular throat shape with results included as Figure 12. Case 17 has the intermediate throat shape. Since only the throat shape was different, results forward of the notch were the same. Downstream of the notch the differences in the results are fairly subtle. There was a trend to lower boundary layer area at the inlet exit as the shape became more elliptical. In addition, the rate of boundary layer growth through the isolator was minimized when the isolator did not change shape. **Cases 13, 14, and 17** illustrate the effects of changing only the throat aspect ratio. For a throat aspect ratio of one the isolator changed shape from a rounded square to a circle as shown in Figure 13. At the inlet exit, each case has the typical three boundary layer “bubbles”. For the large aspect ratio throat geometry Case 14 shown in Figure 14, the body and cowl boundary layers merge at the centerline before the isolator exit. **Cases 11, 12, and 17** show the effects of changing only the capture aspect ratio. For these cases the isolator shape remained the same. As the capture aspect ratio increased (Case 11 Figure 15, Case 17 Figure 10, Case 12 Figure 16) the greater lateral compression increased boundary layer growth. The increased rate of growth continued through the isolator even though the isolator geometry was constant. **Cases 9, 10, and 17** reveal the effects of changing only the lip angle. As the lip angle increased (Case 9 Figure 17 to Case 10 Figure 18) the boundary layer area ratio decreased at the inlet and isolator exits. However, the basic structure of the flowfield was very similar.

Cases 1 – 8 represent extreme cases with every variable at a minimum or maximum value. **Cases 1 and 6** were cases with a constant shape elliptical isolator. Case 1 had a large lip angle and capture aspect ratio with results shown in Figure 19. Case 6 had a small lip angle and capture aspect ratio with results shown in Figure 20. Despite the same shape isolator and nearly equivalent inlet exit boundary layer area ratios, less boundary layer growth through the isolator was predicted for Case 6. Later analysis will show that the lip angle and capture aspect ratio produce opposite effects on the boundary layer area ratio response parameter. However, the capture aspect ratio has greater sensitivity. **Cases 2 and 8** were cases with a constant shape circular isolator. Results for Case 2 are shown in Figure 21 and Case 8 results in Figure 22. Case 2 had a large lip angle and capture aspect ratio, while Case 8 had a small lip angle and capture aspect ratio. Somewhat surprisingly, although the lip angle and capture aspect ratio were at the extremes for this comparison the Mach number contours at the inlet exit are not very different. In both cases the boundary layer consumes just over 60% of the inlet exit area. In contrast, although the isolator shapes were the same, the boundary layer growth through the isolator noticeably increased for the large lip angle and capture aspect ratio (Case 2). **Cases 3 and 7** were cases with a large aspect ratio, highly rectangular inlet exit shape. Case 3 had a large lip angle and small capture aspect ratio with results shown in Figure 23. Case 7 had a small lip angle and large capture aspect ratio with results shown in Figure 24. Although the same shape change occurred through the isolator, a large lip angle and small capture aspect ratio produced a lower inlet exit boundary layer area ratio and also a lower growth rate through the isolator (17% vs. 19.4%). In both cases the body and cowl side boundary layers merged at the centerline before the isolator exit. **Cases 4 and 5** were cases with a nearly square isolator entrance and a circular isolator exit. Case 4 had a small lip angle and large capture aspect ratio with results shown in Figure 25. Case 5 had a large lip angle and small capture aspect ratio with results shown in Figure 26. The small lip angle and large capture aspect ratio of Case 4 combine to produce a higher boundary layer area ratio at the inlet exit. However, despite the same isolator geometry, the boundary layer area ratio through the isolator grows less (17.6%) than Case 5 (19.3%).



P (psi): 1.0 1.3 1.7 2.1 2.8 3.6 4.6 5.9 7.7 9.9 12.7 16.4 21.2 27.3 35.2
Figure 8. Case 17 surface pressure and flow Mach number contours.

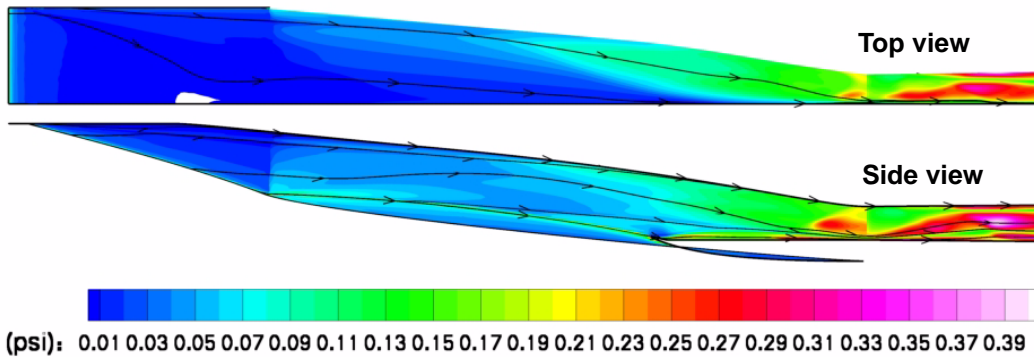


Figure 9. Case 17 surface shear and streamlines (top and side views).

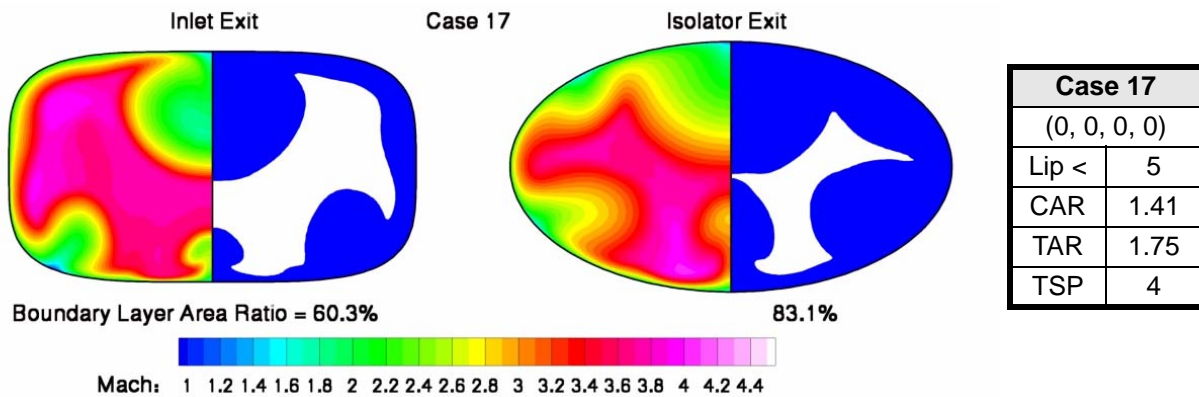
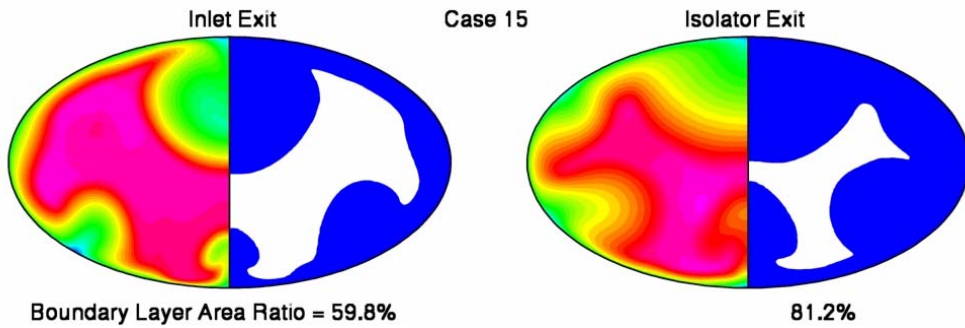
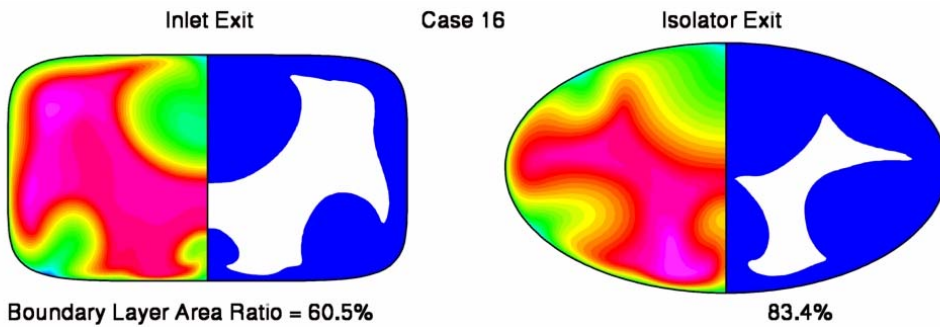


Figure 10. Case 17 Mach number contours and boundary layer shape.



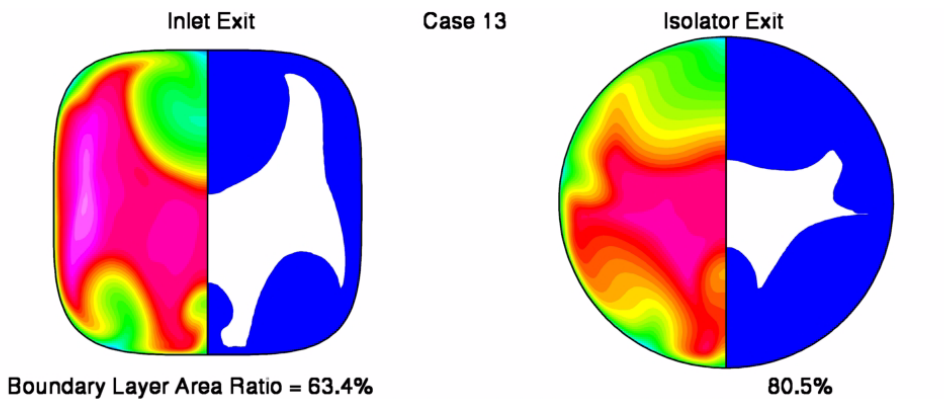
Case 15	
(0, 0, 0, -1)	
Lip <	5
CAR	1.41
TAR	1.75
TSP	2

Boundary Layer Area Ratio = 59.8% 81.2%
Figure 11. Case 15 Mach number contours and boundary layer shape.



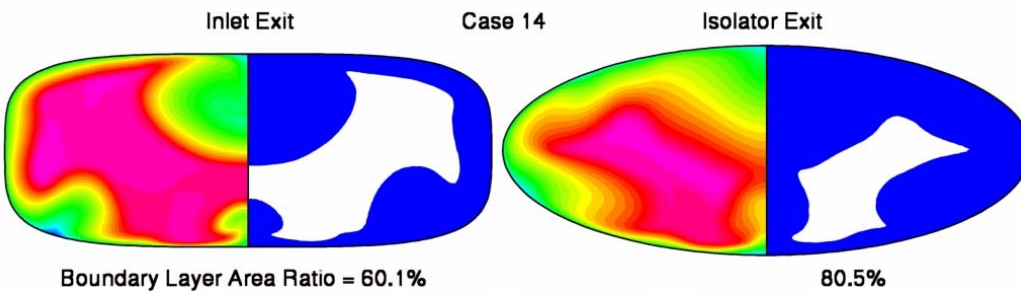
Case 16	
(0, 0, 0, 1)	
Lip <	5
CAR	1.41
TAR	1.75
TSP	6

Boundary Layer Area Ratio = 60.5% 83.4%
Figure 12. Case 16 Mach number contours and boundary layer shape.



Case 13	
(0, 0, -1, 0)	
Lip <	5
CAR	1.41
TAR	1
TSP	4

Boundary Layer Area Ratio = 63.4% 80.5%
Figure 13. Case 13 Mach number contours and boundary layer shape.



Case 14	
(0, 0, 1, 0)	
Lip <	5
CAR	1.41
TAR	2.5
TSP	4

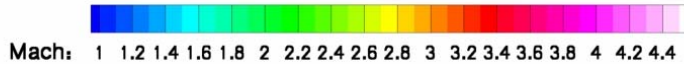


Figure 14. Case 14 Mach number contours and boundary layer shape.

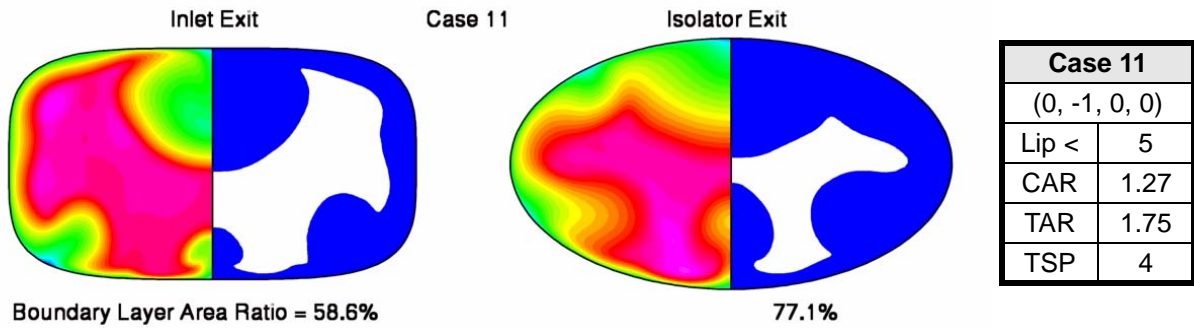


Figure 15. Case 11 Mach number contours and boundary layer shape.

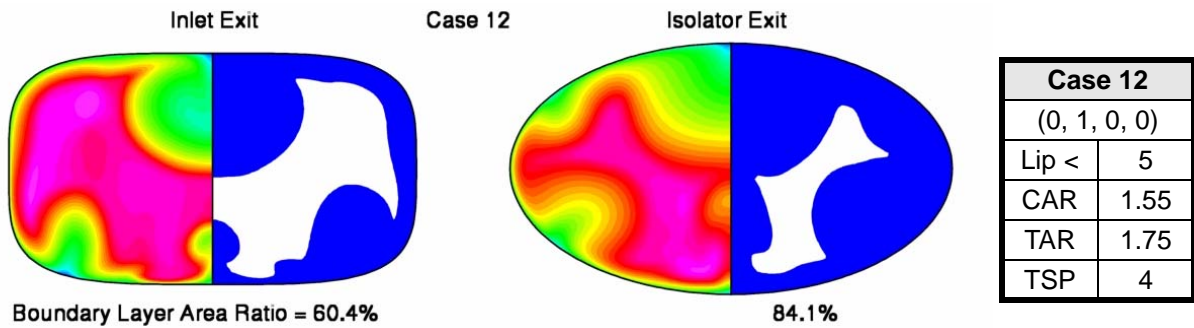


Figure 16. Case 12 Mach number contours and boundary layer shape.

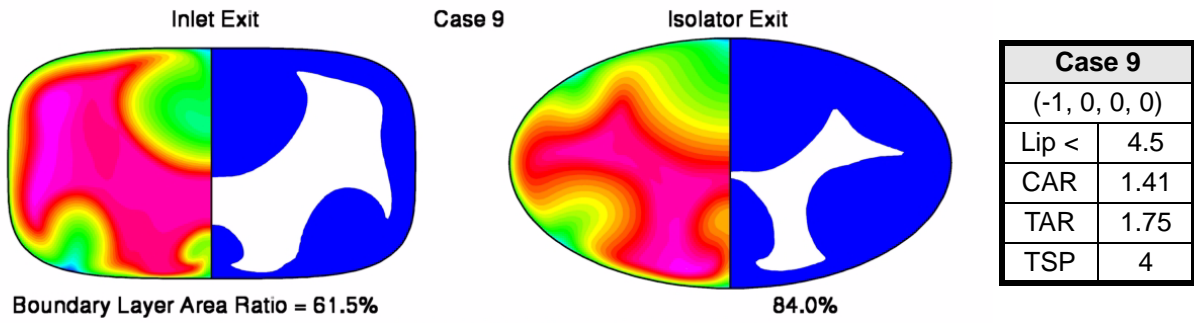


Figure 17. Case 9 Mach number contours and boundary layer shape.

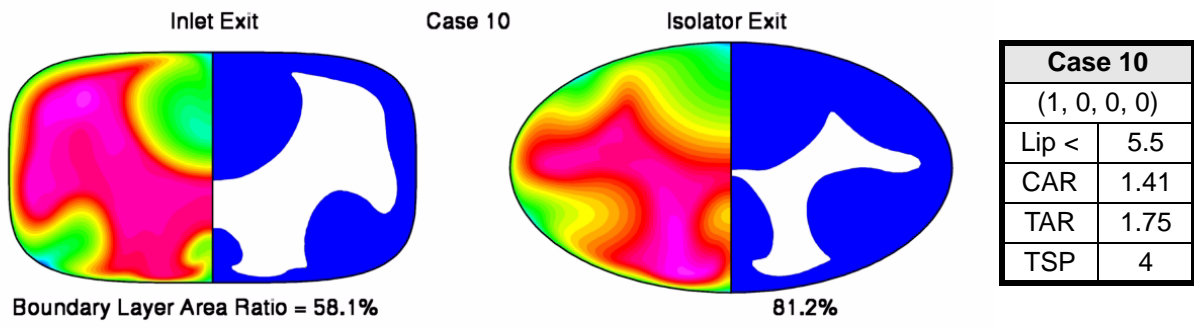


Figure 18. Case 10 Mach number contours and boundary layer shape.

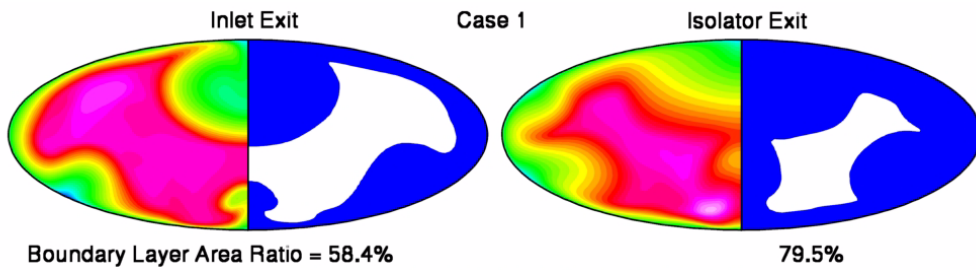


Figure 19. Case 1 Mach number contours and boundary layer shape.

Case 1	
(1, 1, 1, -1)	
Lip <	5.5
CAR	1.55
TAR	2.5
TSP	2

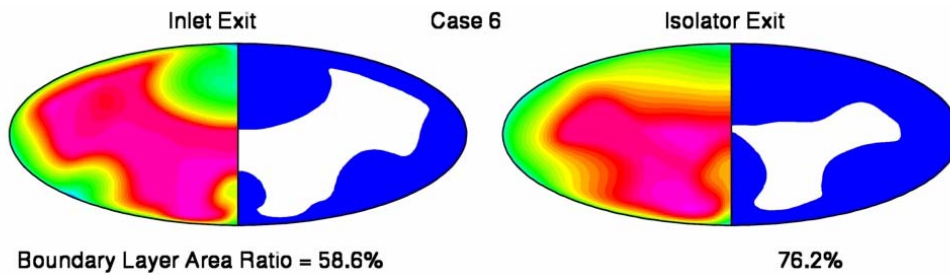


Figure 20. Case 6 Mach number contours and boundary layer shape.

Case 6	
(-1, -1, 1, -1)	
Lip <	4.5
CAR	1.27
TAR	2.5
TSP	2

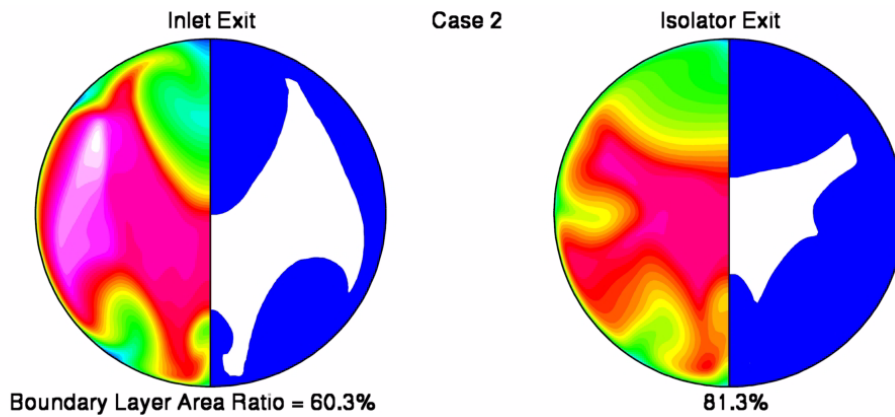


Figure 21. Case 2 Mach number contours and boundary layer shape.

Case 2	
(1, 1, -1, -1)	
Lip <	5.5
CAR	1.55
TAR	1
TSP	2

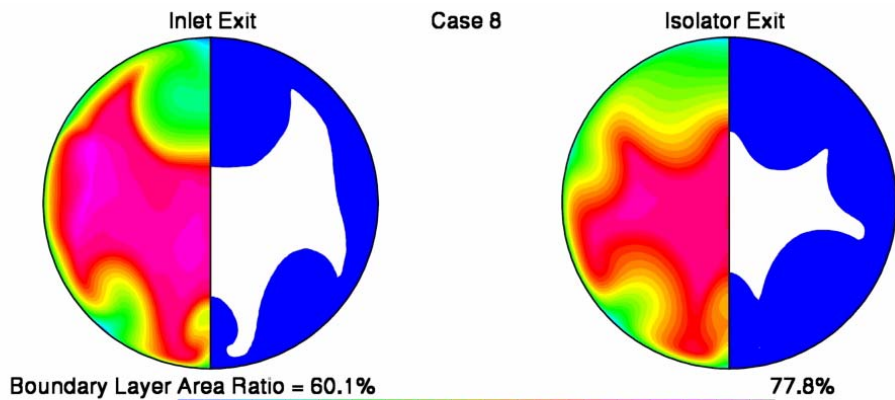


Figure 22. Case 8 Mach number contours and boundary layer shape.

Case 8	
(-1, -1, -1, -1)	
Lip <	4.5
CAR	1.27
TAR	1
TSP	2

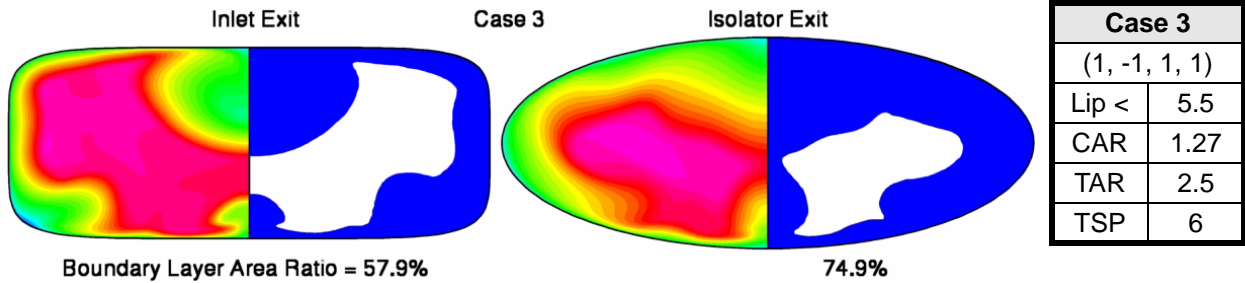


Figure 23. Case 3 Mach number contours and boundary layer shape.

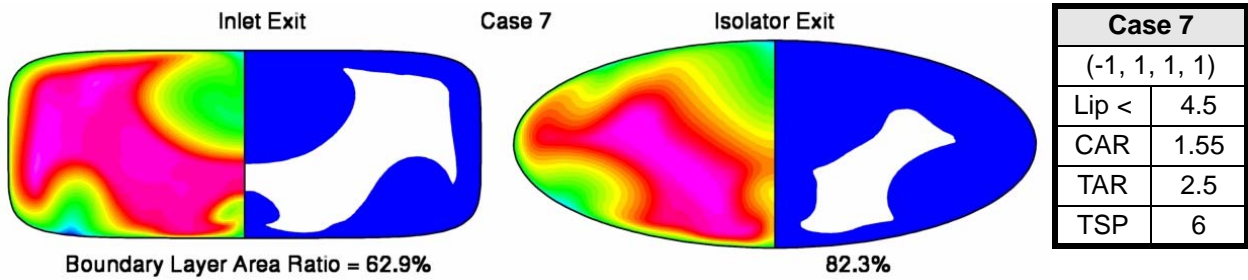


Figure 24. Case 7 Mach number contours and boundary layer shape.

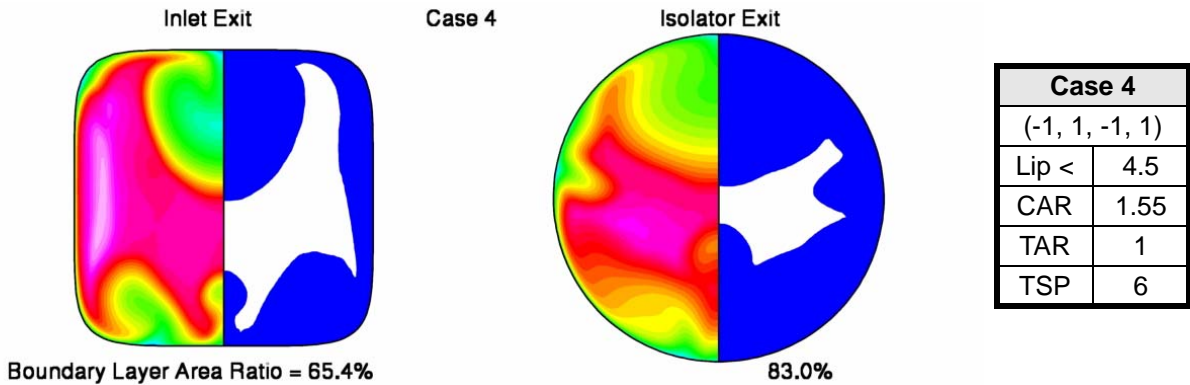


Figure 25. Case 4 Mach number contours and boundary layer shape.

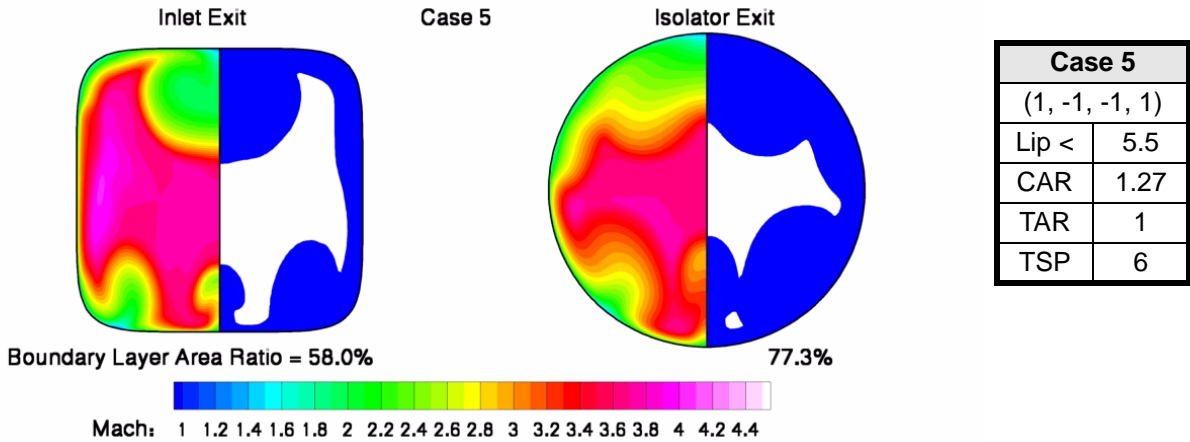


Figure 26. Case 5 Mach number contours and boundary layer shape.

FLOWFIELD ANALYSIS

A series of post-processors were used to extract information from each solution. The purpose was to examine common performance parameters and assess parameters which may correlate with well-behaved boundary layer characteristics.

ONE-DIMENSIONAL FLOW PROPERTIES

A primary method used to compare each complex flowfield is to one-dimensionalize the flowfield at each cross-sectional plane. A flux-conservative algorithm was used.¹¹ One-dimensional flow pressure is plotted in Figure 27 from the notch to the isolator exit. To facilitate comparisons of every case, the inlet exit axial location has been shifted to $X=0$. Since the inlet lengths from the notch to the throat were not the same, the curves do not begin at the same X location. The cases with a throat aspect ratio of 1 exhibit a significantly stronger compression for the first half from the notch to the throat (inlet exit), but then less aggressive compression for the second half (lower slope) than the other cases.

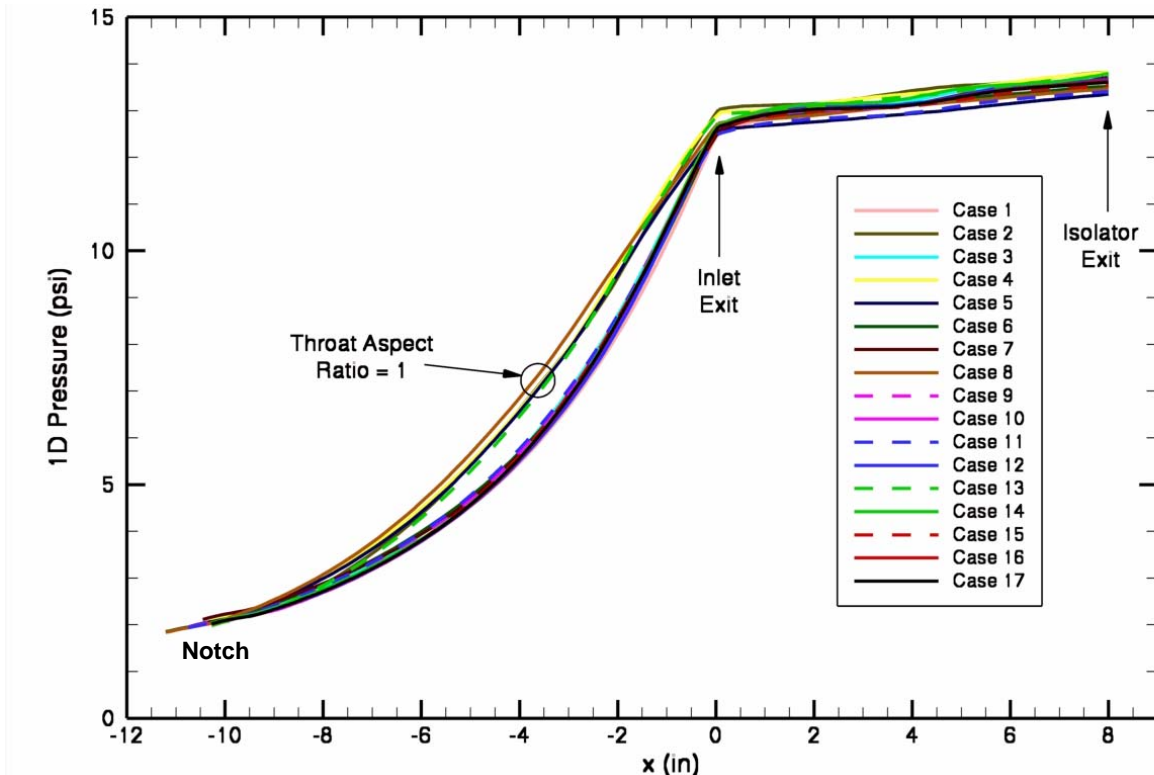


Figure 27. One-dimensional flow pressure.

PERIMETER AVERAGES

A surface quantity post-processor was used to analyze the inlet surface from the notch to the isolator exit. The utility extracted surface information at each axial location. Figure 28 shows the average shear around the perimeter with roughly the same behavior exhibited by every case.

BOUNDARY LAYER AREA RATIO RESULTS

Tecplot¹² was used to sum the area occupied by the boundary layer. The boundary layer edge was defined to be 99.5% of freestream total enthalpy. By performing the summation at every cross-sectional grid plane from the notch aft, a line plot showing the boundary layer growth to the isolator exit could be generated for each case. The results have been divided by the local cross-sectional geometric area to form a boundary layer area ratio (BLAR) and shifted so that $X=0$ is the end of the inlet. The results revealed little sensitivity to throat aspect ratio or superellipse power. The red curves of Figure 29 (plus Case 17) show a small advantage through the inlet and isolator toward the higher lip angle (Case 10). A larger advantage is indicated by the blue curves (plus Case 17), for a small capture aspect ratio (Case 11).

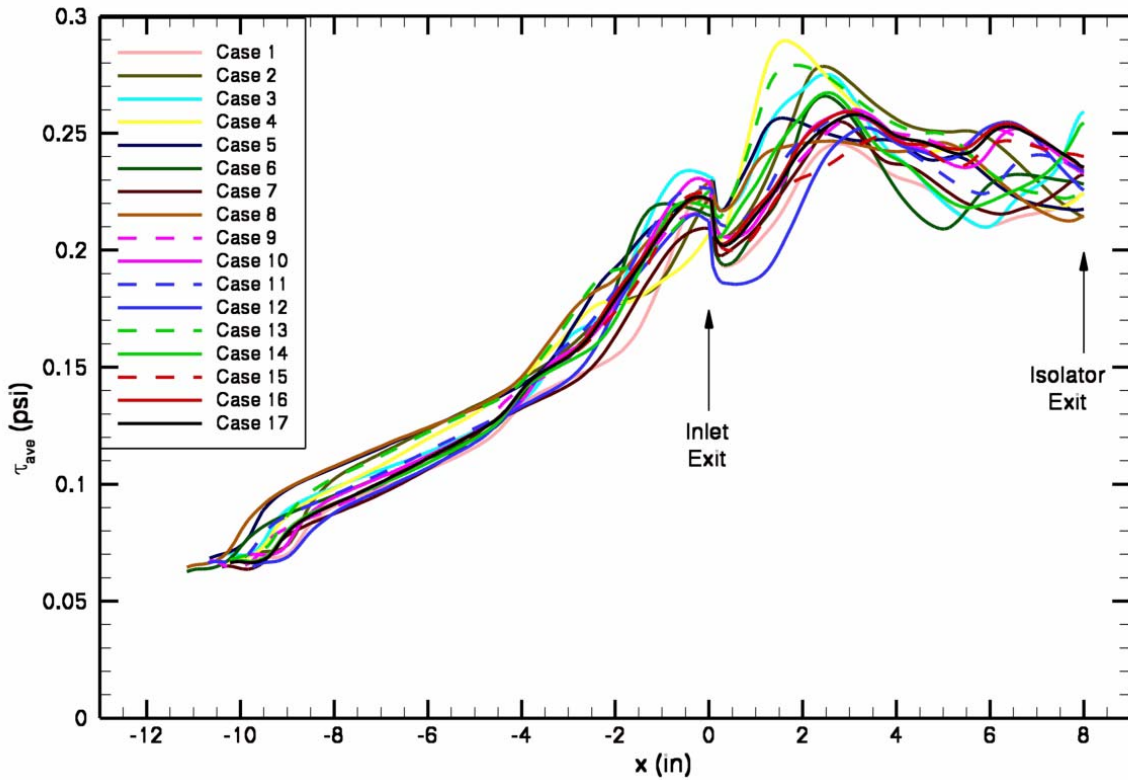


Figure 28. Inlet and isolator circumferential average wall shear.

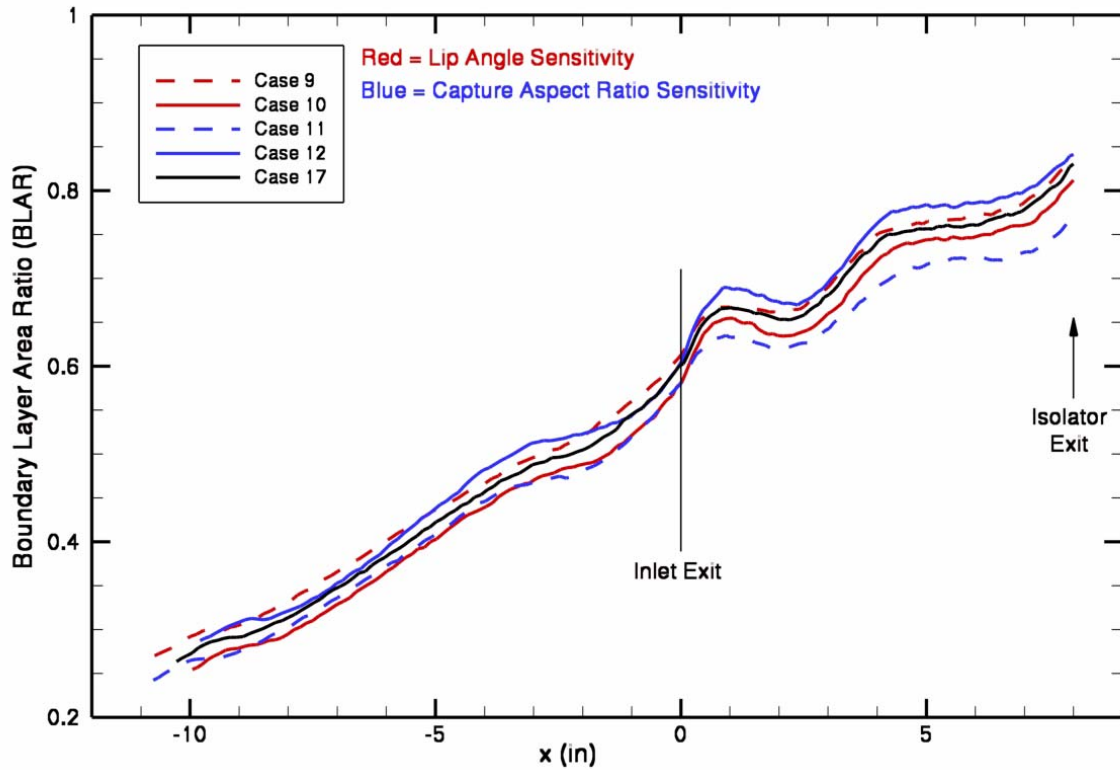


Figure 29. Boundary layer area ratio results for lip angle and capture aspect ratio sensitivity cases.

BODY CENTERLINE PRESSURE AND SHEAR

Figure 30 shows the body centerline wall pressure comparison. After the blunt leading edge, the pressure increases within the first 10 inches due to the effects of the blunt sidewall leading edge and the initial lip angle. The pressure rise due to the notch close-out occurs at approximately -2 inches or just in front of the inlet exit for every case.

Figure 31 shows the body centerline wall shear comparison. Some of the boundary layers separate at the beginning of the body centerline compression. This would not occur if the boundary layer was modeled as fully turbulent. Most cases also exhibit a fairly “weak” boundary layer (approaching separation) at -8 inches or just inside the notch axial location. This particular location of boundary layer “weakness” correlates to the location where the most outboard forebody surface streamline reaches the inlet centerline as shown in the top image of Figure 9. For Case 4, the location of near zero shear moves significantly downstream.

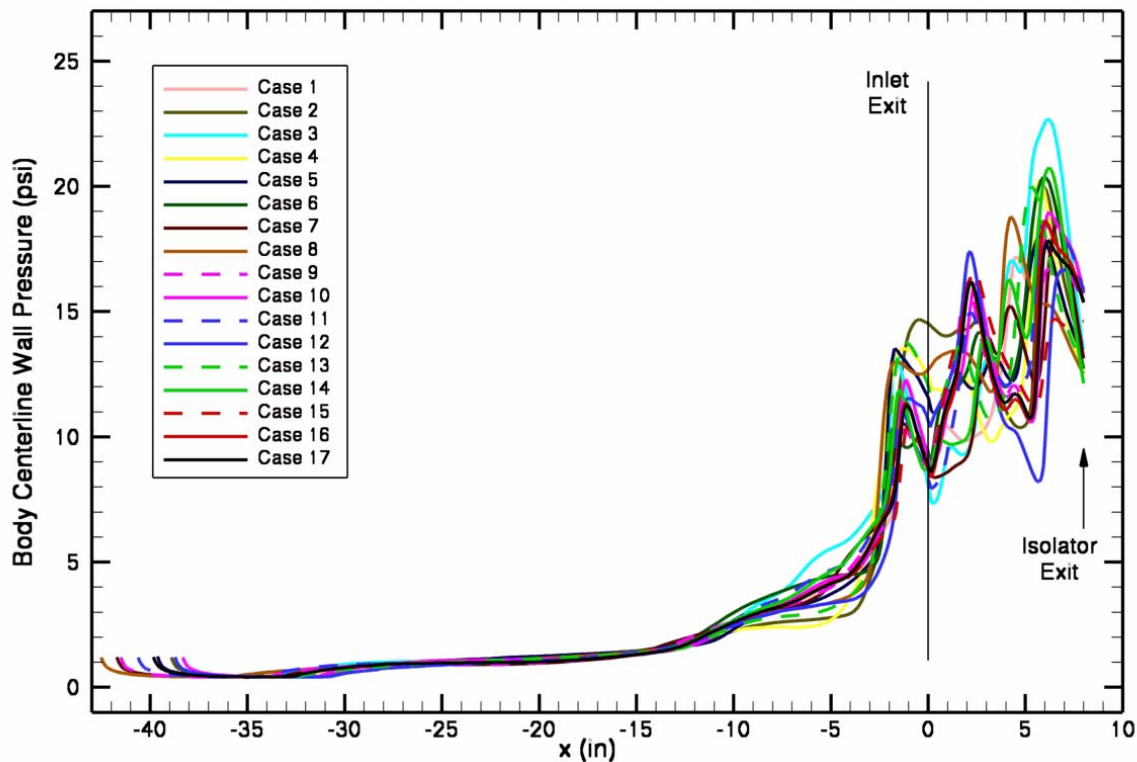


Figure 30. Body centerline wall pressure comparison.

CENTERLINE BOUNDARY LAYER RESULTS

A post-processor utility was used to calculate boundary layer properties along the body and cowl surface centerlines. The results have been colored as in the previous section and shifted so that $X=0$ is the inlet exit. The body and cowl boundary layers merged along the centerline within the isolator for some cases, so boundary layer properties could not be calculated all the way to the isolator exit for those cases. Of the high throat aspect ratio cases (1, 3, 6, 7, 14) only Case 6 did not merge by the isolator exit. The case which merged earliest was Case 7. Only the body centerline results are included in this paper. The boundary layer displacement thickness is plotted in Figure 32. The displacement thickness increases at the notch shock reflection location on the body centerline. The magnitude and rate of change of displacement thickness indicates that the displacement thickness predicted by three-dimensional CFD could not be added to an inviscid design shape to produce a reasonable design.

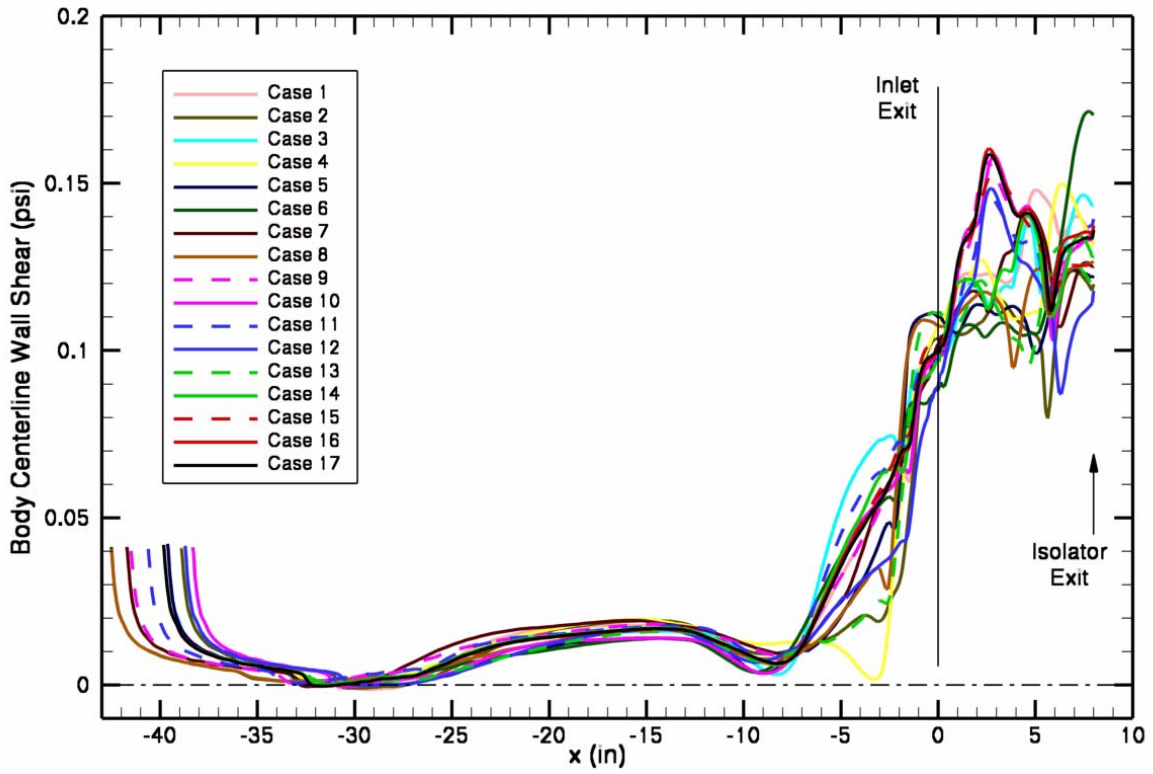


Figure 31. Body centerline shear comparison.

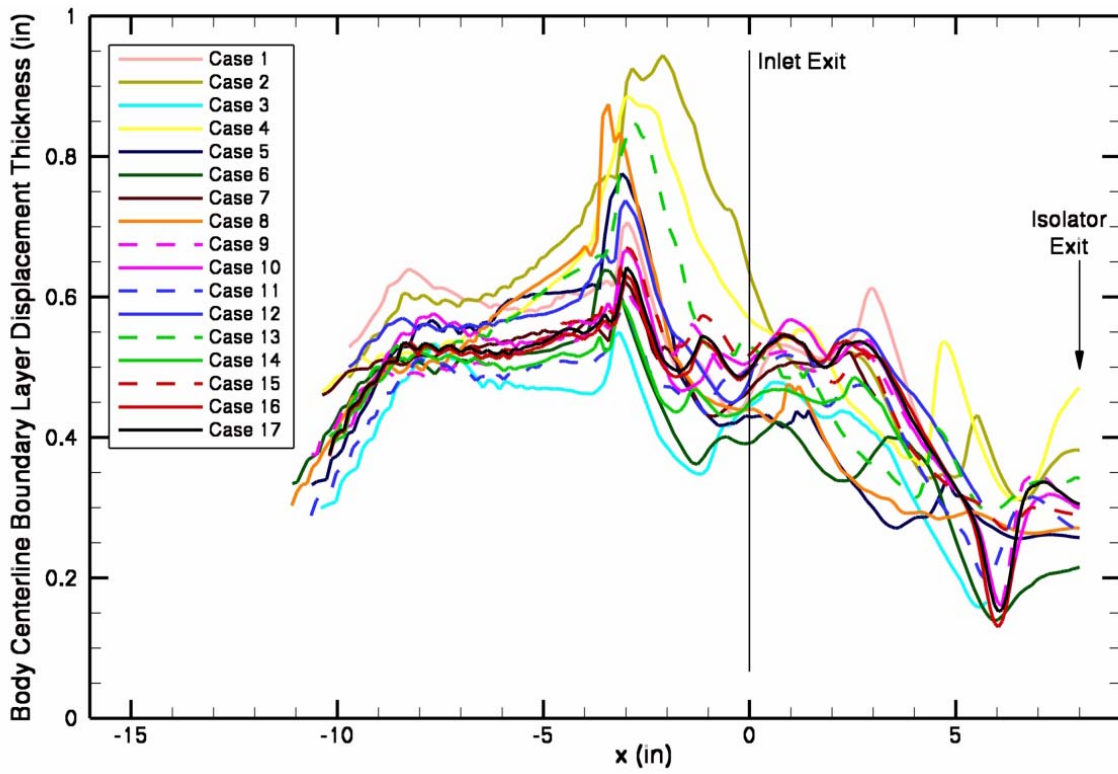


Figure 32. Body centerline boundary layer displacement thickness.

TABULATED PARAMETERS

A large amount of information was extracted from the CFD solution for each case. A range of post-processing utilities were used to calculate: integrated fluxes, one-dimensional flow properties, efficiencies, distortion parameters, centerline surface quantities, surface quantity minimum/average/maximum around the perimeter, and boundary layer properties. A small sample of parameters is listed in Table 3. Determining the sensitivity to the independent variables, including potential two-parameter interactions, would be virtually impossible if the database was not created with a systematic approach. However, since the database was created with a Modern Design of Experiments technique, statistical analysis is relatively straightforward and any output parameter could be part of an optimization function as demonstrated in the following sections.

Table 3. Tabulated parameters.

Case	Total Drag	Wetted Surface Area	Inlet exit body CL boundary layer properties			Isolator exit 1D properties				
			τ	δ	δ^*	Stream Thrust	Mach	η_{KE}	P_t recov	BLAR
			psi	inch						
N	m ²									
1	750	0.3810	0.099	0.841	0.467	3414	3.09	0.9004	0.2854	0.795
2	754	0.3697	0.104	1.197	0.622	3416	3.06	0.9008	0.2764	0.813
3	727	0.3562	0.099	0.740	0.448	3521	3.08	0.9050	0.3492	0.749
4	723	0.3994	0.108	1.079	0.563	3304	3.06	0.8980	0.2695	0.830
5	694	0.3479	0.110	0.838	0.429	3498	3.13	0.9100	0.3580	0.773
6	692	0.3862	0.089	0.677	0.392	3435	3.10	0.9052	0.3490	0.762
7	721	0.4096	0.102	0.809	0.474	3275	3.07	0.8951	0.2682	0.823
8	682	0.3745	0.107	0.883	0.441	3439	3.11	0.9087	0.3528	0.778
9	691	0.3830	0.096	0.880	0.502	3263	3.09	0.9013	0.3118	0.840
10	707	0.3474	0.099	0.875	0.508	3310	3.09	0.9036	0.3211	0.812
11	684	0.3598	0.098	0.840	0.498	3398	3.12	0.9070	0.3472	0.771
12	685	0.3621	0.089	0.845	0.481	3091	3.08	0.8985	0.2796	0.841
13	697	0.3591	0.112	0.984	0.528	3304	3.07	0.9034	0.3148	0.805
14	705	0.3691	0.097	0.762	0.453	3271	3.06	0.8992	0.3064	0.805
15	693	0.3637	0.102	0.934	0.520	3286	3.10	0.9040	0.3201	0.812
16	699	0.3480	0.099	0.874	0.498	3280	3.09	0.9022	0.3147	0.834
17	697	0.3642	0.099	0.882	0.499	3280	3.09	0.9027	0.3159	0.831

RESPONSE PARAMETER REGRESSION EQUATIONS

The generation of regression equation coefficients could be attempted for any tabulated response parameter. However, this effort is best limited to responses with a variation that the user reasonably believes could be fit with a second order function. Therefore, integrated properties are better suited for this type of analysis than discrete properties. Design Expert software was used to analyze three response parameters: total drag, total pressure recovery at the isolator exit, and boundary layer area ratio (BLAR) at the isolator exit. The results of the software were coefficients of a second order function of the normalized independent variables as shown in Equations 2 – 6. The coefficients are listed in Table 4. A general feel for the character of the equation can be achieved by generating one-variable-at-a-time permutation plots. These are generated by holding three variables fixed and sweeping the remaining variable from its minimum to maximum value. When the results for each variable are plotted together the character and sensitivity of the selected response to the variation of each independent variable is revealed.

$$\text{Response} = C_1 + C_2A + C_3B + C_4C + C_5D + C_6AB + C_7AC + C_8AD + C_9BC + C_{10}BD + C_{11}CD + C_{12}A^2 + C_{13}B^2 + C_{14}C^2 + C_{15}D^2 \quad (2)$$

$$A = \frac{\text{Lip Angle} - 5}{0.5}, 4.5 \leq \text{Lip Angle} \leq 5.5 \quad (3)$$

$$B = \frac{\text{Capture Aspect Ratio} - 1.41}{0.14}, 1.27 \leq \text{Capture Aspect Ratio} \leq 1.55 \quad (4)$$

$$C = \frac{\text{Throat Aspect Ratio} - 1.75}{0.75}, 1 \leq \text{Throat Aspect Ratio} \leq 2.5 \quad (5)$$

$$D = \frac{\text{Throat Superellipse Power} - 4}{2}, 2 \leq \text{Throat Superellipse Power} \leq 6 \quad (6)$$

Table 4. Response equation coefficients.

Coefficient	Total Drag	Pt Recovery	BLAR
C1	688.73	0.31498	0.82471
C2 (A)	8.07	3.88E-3	-0.01380
C3 (B)	0.36	-3.38E-2	0.03500
C4 (C)	4.48	-1.33E-3	-0.00658
C5 (D)	2.84	-2.41E-3	0.01105
C6 (AB)	4.32	0	0.0077
C7 (AC)	2.68	0	0
C8 (AD)	-18.78	4.89E-3	0.01020
C9 (BC)	-6.19	2.54E-3	0
C10 (BD)	-5.36	0	-0.0061
C11 (CD)	3.24	-1.91E-3	0
C12 (A ²)	9.69	1.62E-3	0
C13 (B ²)	0	-1.43E-3	-0.01654
C14 (C ²)	12.39	-4.23E-3	-0.01814
C15 (D ²)	6.99	2.57E-3	0

MULTI-PARAMETER OPTIMIZATION FUNCTION

Even though all cases in the database displayed significant boundary layer roll-up and low isolator entrance wall shear, an initial optimization process within the current design space was performed. In the future the design space will be expanded beyond what is possible with the inviscid design tool with the intent of optimizing to a high efficiency, high back pressure capable design. Any performance parameter can be optimized. However, since a single performance parameter is rarely sufficient to capture all trade-offs and different performance parameters can produce conflicting design trends, construction of a function of multiple performance parameters was proposed prior to optimization. The available performance parameters depend upon the type of design study. If the inlet had been part of a flowpath design study, than vehicle level performance parameters could be considered. For this study (inlet component only with equal mass capture and overall compression), a function with three terms was constructed. The first term was a vehicle integration parameter to include external cowl drag. The second term represented the efficiency of the inlet compression. The third term attempted to quantify the quality of the inlet exit flow from a viscous or operability range perspective. The inlet total drag, one-dimensional total pressure

recovery, and boundary layer area ratio at the end of the isolator were selected for the following example. Finally, the relative significance of each performance parameter must be controllable. This was achieved by normalizing each parameter as shown in Equation 7.

$$\text{If parameter min is desired: } \frac{\text{High} - \text{Value}}{\text{High} - \text{Low}} \quad \text{If parameter max is desired: } \frac{\text{Value} - \text{Low}}{\text{High} - \text{Low}} \quad (7)$$

Therefore, for this example the multi-parameter performance function became:

$$P = A \frac{754 - \text{Drag}}{754 - 674} + B \frac{P_{t(\text{recov})} - 0.268}{0.360 - 0.268} + C \frac{0.855 - \text{BLAR}}{0.855 - 0.700} \quad \text{with } A=B=C=1/3 \quad (8)$$

for a total possible range of 0 to 1. However, since all individual parameters were not minimized or maximized at the same design, the actual range was 0.13 to 0.81. In this example each term was weighted equally. However, the coefficients could be weighted to vary the importance of each term. The one-variable-at-a-time permutation plot about the center of the design space for the multi-parameter performance function is shown in Figure 33. This plot shows the relative importance of the variation of each independent variable with a second order model. However, no two parameter interaction effects are included. It suggests that the optimum will occur at intermediate values for the lip angle and throat aspect ratio (black and green) and at the minimum values for the capture aspect ratio and the throat superellipse power (red and blue). The sensitivity to the capture aspect ratio was greater than for any other variable. The optimum of the multi-parameter performance function was (-0.4, -1, -0.3, -1) for a lip angle of 4.8 degrees, capture aspect ratio of 1.27, throat aspect ratio of 1.525, and throat superellipse power of 2 (true ellipse). Interestingly, the worst design in terms of the multi-parameter performance function was Case 2 (1, 1, -1, -1). Therefore, a true ellipse throat shape was part of the best and worst designs.

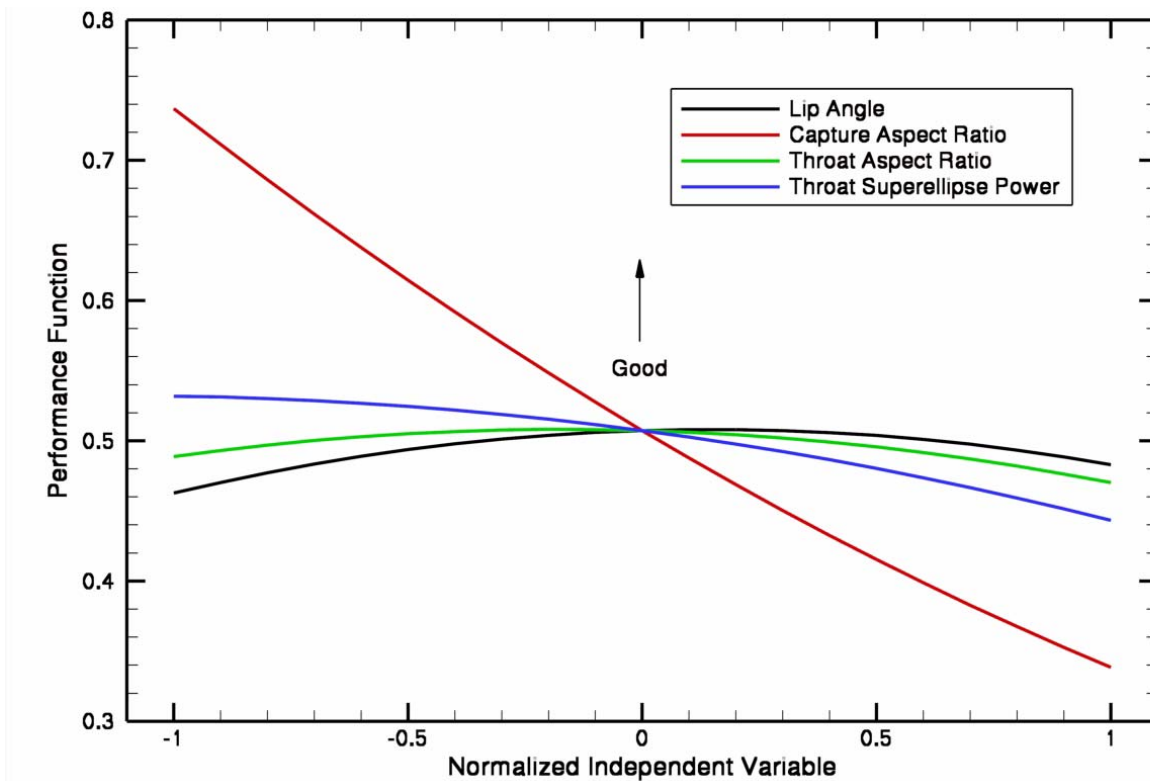


Figure 33. Multi-parameter performance function permutation at the center of the design space.

One-variable-at-a-time permutation plots centered at the optimum design were generated for each individual performance parameter. Since none of the optimum values were at the center of the design space, two-parameter interaction terms could become significant depending upon the magnitude of the coefficients. Figure 34 shows the total drag permutation about the multi-parameter performance function optimum. Total drag would be minimized at an intermediate value for throat aspect ratio and at the minimum for all other variables. A nearly linear sensitivity is predicted for the capture aspect ratio. At this location in the design space, the lip angle variation produced the greatest change in total drag. The isolator exit total pressure recovery permutation at the performance function optimum is shown in Figure 35. The linear coefficient for the capture aspect ratio (B) is an order of magnitude larger than any other coefficient. Therefore, the near linear sensitivity to capture aspect ratio is greater than the sensitivity to all other variables combined. The boundary layer area ratio permutation at the performance function optimum is shown in Figure 36. Interestingly, the optimum throat aspect ratio in terms of the performance function (-0.3 on green line) is near the worst (highest point) in terms of the BLAR. It is a good example of one performance parameter being over-powered by the other two. Stronger weighting of BLAR and lowering the importance of total drag would lead to an optimum with a higher lip angle and throat aspect ratio.

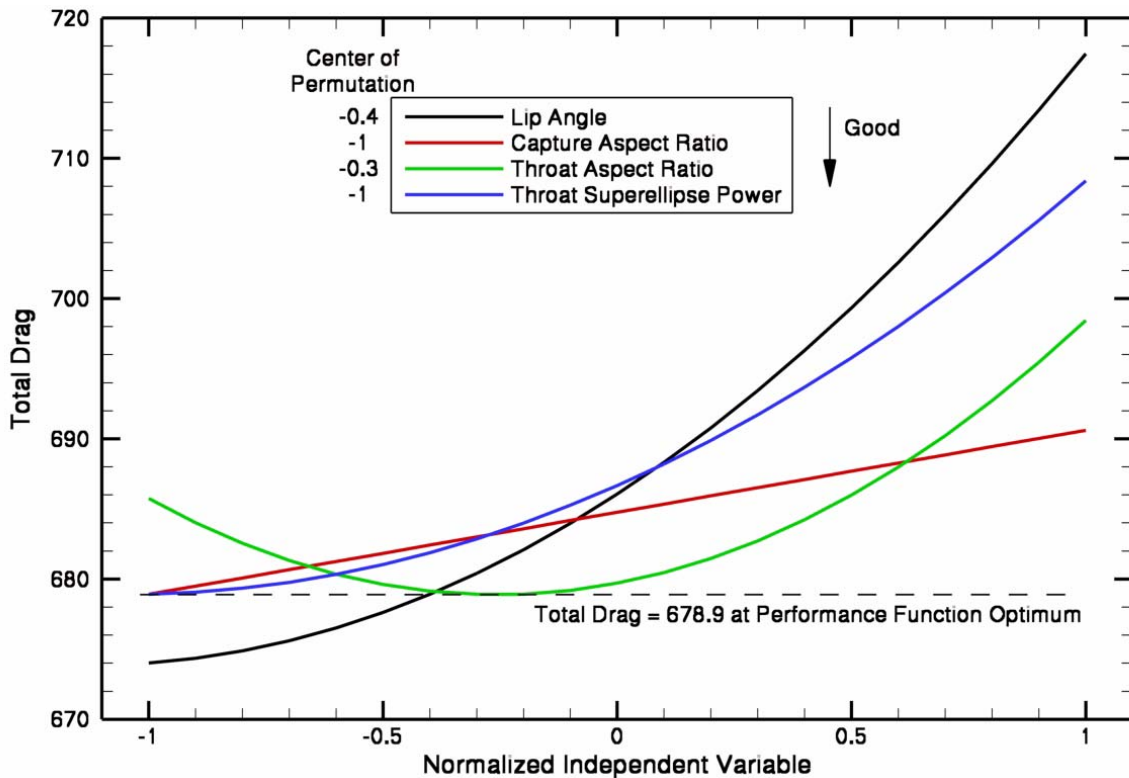


Figure 34. Total drag permutation centered at the performance function optimum.

Figure 37 shows the permutation plot of the multi-parameter performance function centered at the optimum design. A fairly shallow optimum is indicated for the variables which optimized within the design space (lip angle and throat aspect ratio). For example, a design with a circular throat (normalized throat aspect ratio = -1) would only suffer a small penalty. The greater sensitivity to throat superellipse power than to throat aspect ratio is fairly surprising and perhaps some skepticism is appropriate (recalling the “small” MDOE matrix). Nevertheless, an optimized throat superellipse power of 2 (normalized = -1) and the slope of the blue line suggest a significant benefit to performing all of the shape change in the inlet with a constant shape isolator. For the ranges of the independent variables and selected performance function, the capture aspect ratio was the most sensitive independent variable with a preference to a small capture aspect ratio.

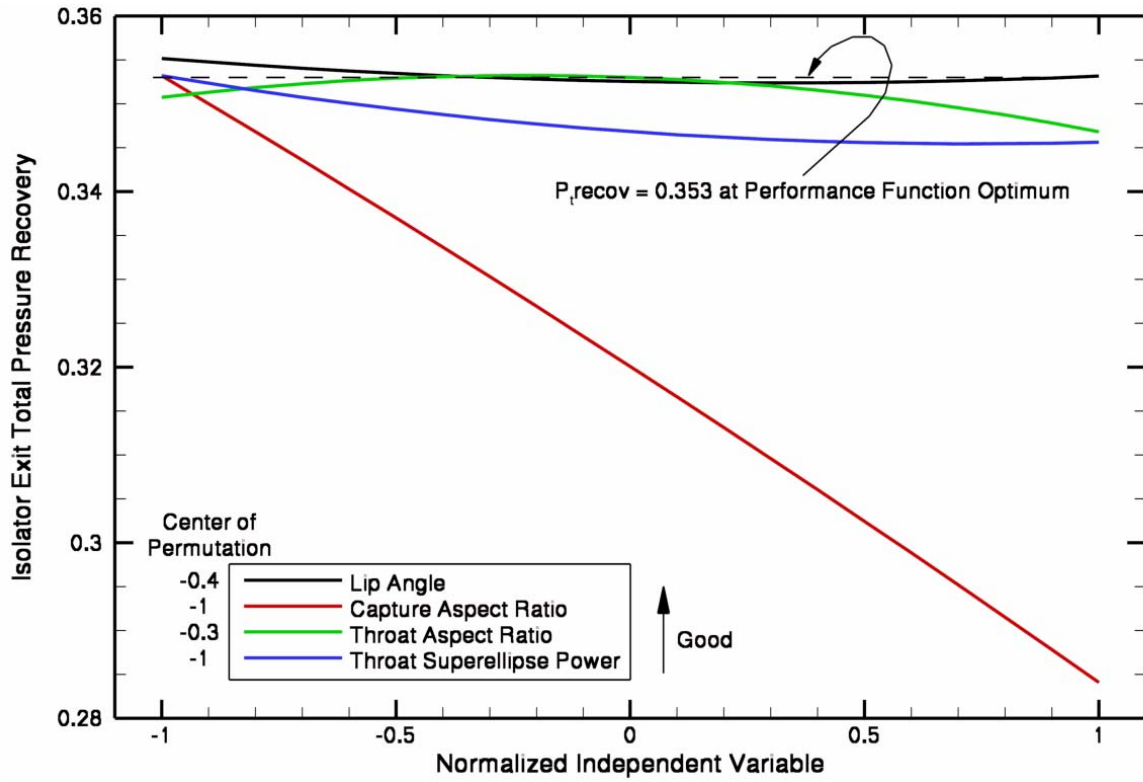


Figure 35. Total pressure recovery permutation centered at the performance function optimum.

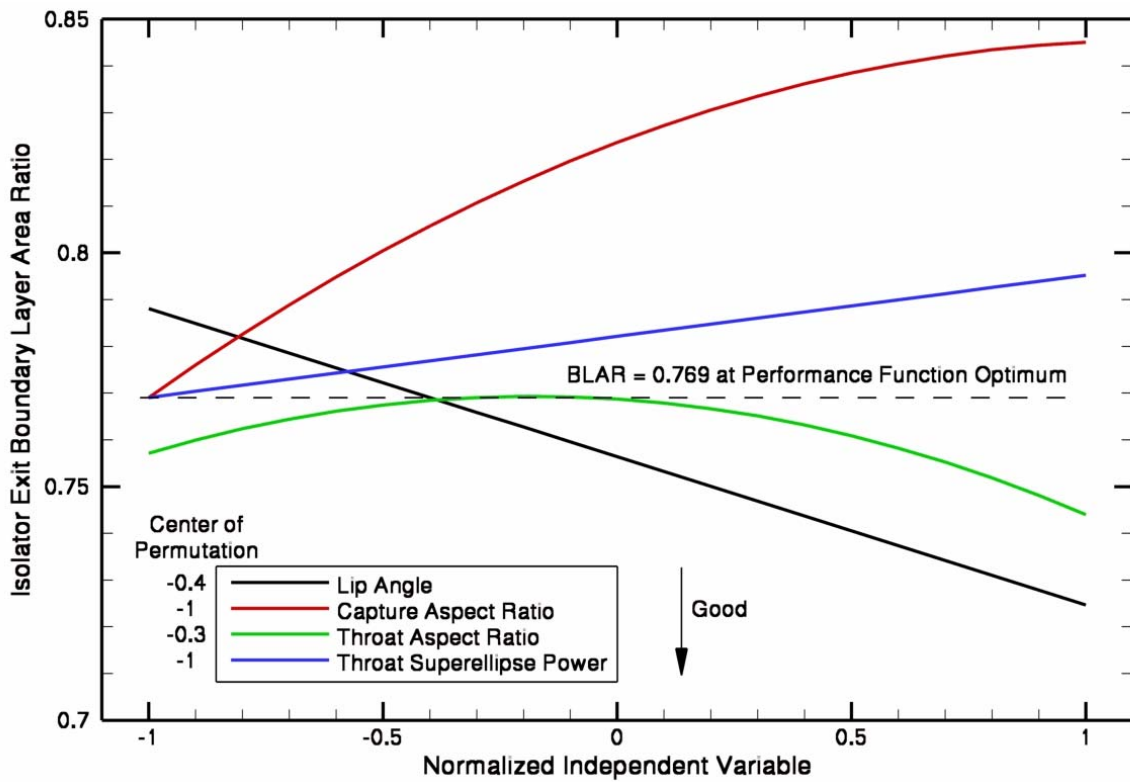


Figure 36. Boundary layer area ratio permutation centered at the performance function optimum.

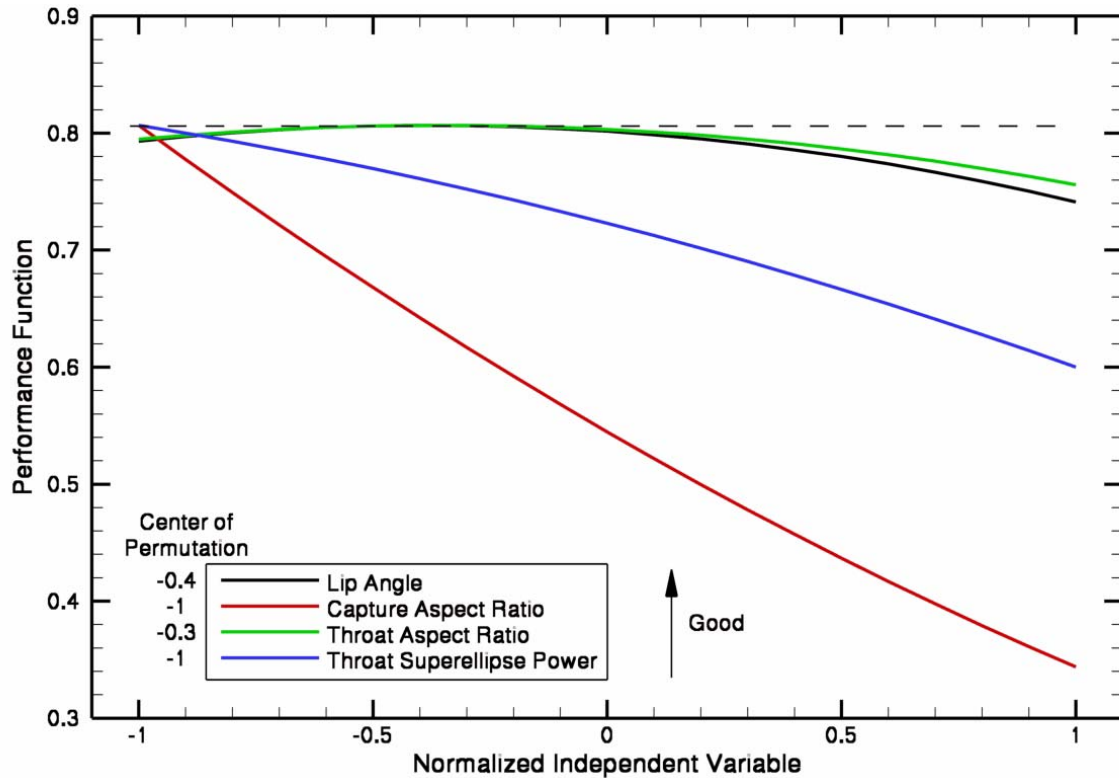


Figure 37. Performance function permutation centered at the performance function optimum.

DESIGN STUDY CONCLUSIONS

An initial design study for REST-class three-dimensional inlets was performed to drive the development of parametric geometry and structured grid generation tools and to generate data to assess performance parameters, particularly for viscous effects. Four geometric variables used by an inviscid design tool were investigated. Results from the initial study suggest that no shape change should occur through the isolator. The capture aspect ratio should remain an independent variable because it controls the amount of lateral compression. The lip angle revealed an interesting trade-off between drag and boundary layer area, so it, or a length variable, should continue to be investigated. The throat aspect ratio was not a strong inlet performance variable and could be constrained by the combustor design. Future CFD-based design efforts will vary geometric features which are part of the surface parameterization, but not possible with the inviscid design tool, and attempt to overcome the viscous flow problems symptomatic of the inviscid design approach.

SUMMARY

A process to increase the use of high-fidelity viscous three-dimensional CFD as a design tool has been developed. It relies on parametric geometry generation linked to structured grid topology generation. This facilitates the rapid creation of geometry and structured grids for CFD analysis. In order to achieve the optimum flow quality from a three-dimensional inlet, a design technique which takes into account the fully coupled behavior of the flow is required. Therefore, an inlet design capability was selected as the first application of this process. The first type of inlet selected was the REST-class hypersonic inlet. An inviscid design tool produced a sample geometry which guided parameterization of the surface. Even though significant flow quality problems were expected, it was used to rapidly create geometries which systematically varied four geometry variables. A parametric CAD model was used to create a continuous surface for each case. Rapid structured grid generation was facilitated by an approach focused on grid

topology. A single grid topology was created and applied to each case. A Modern Design of Experiments approach was used to investigate the design space. The ability to quantify a parameter representative of viscous effects and formulate a relationship to the independent design variables was demonstrated. The new design and analysis capability took 8 days to produce results for 17 cases including geometry and grid generation. The actual CFD solution time was essentially negligible, since many solutions (number of processors / 7) could have been performed simultaneously each day. Therefore, human involvement in the logistics of performing the analysis was still the limiting factor, but was significantly improved over what has been previously possible. Future efforts will continue to streamline various steps and reduce human involvement in tedious tasks. However, as was desired, most of the time was spent analyzing the flowfields, processing performance parameters, and performing a sample optimization. The same design process will be applied to different classes of hypersonic inlets and other components.

ACKNOWLEDGMENT

The authors would like to thank Hilmi Alkawahwi of TechnoSoft, Inc. for the programming necessary to create the parametric geometry within AML.

REFERENCES

- 1). Smart, M.K., "Design of Three-Dimensional Hypersonic Inlets with Rectangular-to-Elliptical Shape Transition", *Journal of Propulsion and Power*, 15(3): 408-416, 1999.
- 2). Barger, Raymond, "A Procedure for Designing Forebodies With Constraints on Cross-Section Shape and Axial Area Distribution", NASA Technical Paper 1881, July 1981.
- 3). AML (Adaptive Model Language) from TechnoSoft, Inc., Cincinnati, OH, <http://www.technosoft.com>.
- 4). GridPro, Program Development Corporation, White Plains, NY, <http://www.gridpro.com>.
- 5). Gridgen, Pointwise, Inc., Fort Worth, TX, <http://www.pointwise.com/gridgen>.
- 6). Ferlemann, P.G., "Forebody and Inlet Design for the HIFiRE 2 Flight Test", JANNAF Propulsion Meeting, Boston, MA, May, 2008.
- 7). Ferlemann, P.G., "HIFiRE 2 Forebody and Inlet Analysis at Nominal Conditions for the 9 Inch Capture Design", Technical Note 09-531, NASA LaRC Contract NNL07AA00B (also HIFiRE Flight 2 Technical Note HF2-TN-004), August 29, 2009.
- 8). Design Expert® Version 7.1.6, Stat-Ease, Inc., Minneapolis, MN, <http://www.statease.com>.
- 9). VULCAN home page, <http://vulcan-cfd.larc.nasa.gov>, September 2009.
- 10). Venkatakrisnan, V., "On the Accuracy of Limiters and Convergence to Steady State Solutions", AIAA Paper 93-0880, January 1993.
- 11). Meyer, Ben, "User Manual and Methodology for One-Dimensionalization Code: Massflow3d version 8.4", Technical Note 06-474, NASA Langley Contract NAS1-00135B, May 11, 2006.
- 12). Tecplot 360, Tecplot, Inc., Bellevue, WA, <http://www.tecplot.com>.